AGU ADVANCING EARTH AND SPACE SCIENCES

AGU Advances

RESEARCH ARTICLE

10.1029/2026AV002429

Irreversible Stirring and Mixing of Tracers by Oceanic Internal Gravity Waves

C. P. Sanjay[1] **and Jim Thomas**[1,2]

[1]International Centre for Theoretical Sciences, Tata Institute of Fundamental Research, Bangalore, Karnataka, India, [2]Centre for Applicable Mathematics, Tata Institute of Fundamental Research, Bangalore, Karnataka, India

Peer Review The peer review history for this article is available as a PDF in the Supporting Information.

Key Points:

- A single plane wave only moves tracers back and forth whereas two plane waves propagating in different directions can induce irreversible tracer stirring
- Increasing the number of plane waves in the flow monotonically enhances stirring and mixing of the tracer field
- Tracer dispersion enhances also with increasing wave amplitude, this being observed in kinematic and dynamic models

Supporting Information:

Supporting Information may be found in the online version of this article.

Correspondence to:

J. Thomas,
jimthomas.edu@gmail.com

Citation:

Sanjay, C. P., & Thomas, J. (2026). Irreversible stirring and mixing of tracers by oceanic internal gravity waves. *AGU Advances*, *7*, e2026AV002429. https://doi.org/10.1029/2026AV002429

Received 11 MAR 2026
Accepted 28 JUN 2026

Abstract Oceanic internal waves are often thought to be ineffective in stirring and mixing tracer fields such as heat, salt, carbon, and other nutrients. Due to their oscillatory nature, waves are expected to merely displace tracers periodically around their mean position. However, observations of enhanced lateral tracer dispersion at submesoscales (<10 km), where energetic internal waves are abundant, urge better understanding of the role of waves in dispersing oceanic tracers. Using theoretical and numerical methods, this study examines the impact of waves and their amplitudes on the lateral dispersion of passive tracers. We show that two or more waves can irreversibly stir and mix tracers. A broadband spectrum of waves further enhances stirring and mixing. Tracer dispersion in general is seen to become more efficient with increasing amplitude of waves. These findings stem from kinematic non-interacting waves and dynamic nonlinearly interacting waves. Our results highlight the effectiveness of finite-amplitude internal waves in tracer stirring and underscore the need to resolve or parameterize wave-induced lateral mixing in large-scale ocean models.

Plain Language Summary Oceanic internal waves are often thought to be poor at mixing heat, salt, carbon, oxygen, and nutrients in the water. This idea comes from the belief that a single wave can only move these tracers back and forth, without actually spreading them out. However, real ocean data and numerical models show that mixing is stronger at small scales, less than 10 km, where internal waves are common. Even so, it's still unclear whether these internal waves truly help spread tracers around. In this study, we look closely at how waves affect the movement of tracers in wave-rich environments using both kinematic and dynamic models. We find that two plane waves moving in different directions can cause irreversible mixing of tracers. When we add more waves and increase their amplitudes, mixing becomes stronger. We also use two dynamic models that can mimic real ocean wave conditions. Tracers in these flows are dispersed and mixed effectively and increasing wave amplitudes showed enhancement in tracer dispersion. These results suggest that wave effects are more important for lateral stirring and mixing than was previously thought, and should be included in large-scale ocean models to improve accuracy.

1. Introduction

Oceanic flows span nearly eight decades of spatial scales, from basin-scale motions spanning thousands of kilometres where the flow is energized to centimetre-scale motions where the flow energy is dissipated. The turbulent flow is involved in transporting and dispersing tracers such as salinity, temperature, carbon, oxygen, and other nutrients introduced at large scales, cascading them across decades of scales before they mix at the smallest diffusive scales. This tracer transfer and mixing occur both along and across surfaces of constant density, referred to as isopycnal and diapycnal mixing, respectively. Diapycnal dispersion and mixing involve departure from geostrophic and hydrostatic balances, with intermittent patches of small-scale turbulence caused by internal wave breaking that drives the mixing process (Gregg et al., 2003; N. Jones et al., 2020; Katsumata et al., 2021; Kunze, 2017; J. R. Ledwell et al., 2011; Müller & Briscoe, 2000; Naveira Garabato et al., 2004; Waterhouse et al., 2014; Whalen et al., 2020; Whitwell et al., 2024). In contrast, isopycnal mixing is prominent at large scales where balances are dominant and mesoscale eddies are thought to be the primary drivers (R. Abernathey et al., 2022; J. Ledwell et al., 1993; J. R. Ledwell et al., 1998). In coarse resolution global ocean models, the stirring effects of these eddies are typically parameterized through prescribed isopycnal diffusivity values (Gent & McWilliams, 1990; Redi, 1982). Observations and numerical analyses reveal pronounced spatial and seasonal variations in isopycnal diffusivity (R. P. Abernathey & Marshall, 2013; Zhurbas & Oh, 2004), and these variations have been shown to strongly influence oceans' carbon uptake, the ventilation of low-oxygen waters, and large-scale circulation patterns (Booth & Kamenkovich, 2008; Gnanadesikan et al., 2013, 2015; Holmes et al., 2022; C. Jones & Abernathey, 2019; McWilliams, 2008). While different pragmatic approaches are used in models, at present there is no clear consensus on the appropriate isopycnal diffusivity values or the suitable three-dimensional spatial structure for the diffusivity field required to capture isopycnal mixing in coarse-resolution global ocean models (Holmes et al., 2022).

Going below mesoscales, considerable lateral tracer stirring occurs at submesoscales, as revealed through several observational campaigns (Balwada et al., 2024; J. R. Ledwell et al., 1998; Klymak et al., 2015; Kunze et al., 2015; Shcherbina et al., 2015; Spiro Jaeger et al., 2020). For example, while analyzing the variance of spice, a passive tracer field formed by the linear combination of temperature and salinity, Spiro Jaeger et al. (2020) observed a steep spectra for the variance of spice, indicating enhanced stirring and mixing of spice. Furthermore, studies of upper-ocean thermohaline structures found more efficient tracer stirring at submesoscales than those predicted by quasi-geostrophic theory (Cole & Rudnick, 2012; Cole et al., 2010; Ferrari & Rudnick, 2000). Although these investigations are unable to pinpoint the precise causes of enhanced stirring effects seen at submesoscales, stirring by ageostrophic flow components, including internal gravity waves, is considered to be one of the possible causes. This hypothesis of enhanced stirring by internal waves at submesoscales also correlates with in situ measurements and satellite altimetry data sets from the past few decades indicating that energetic internal waves are prevalent at submesoscales in many regions of the world's oceans (M. H. Alford, 2003; Lien & Sanford, 2019; Pinkel, 2014; Qiu et al., 2018; Tchilibou et al., 2018; Torres et al., 2018; Vladoiu et al., 2024; Watanabe & Hibiya, 2002).

Despite repeated confirmations on the existence of energetic internal waves at submesoscales, the impact waves have on tracer stirring has been conventionally considered to be weak. Because of the oscillatory nature, wave fields are generally assumed to merely move tracers back and forth about their mean position, producing no net transport at leading order (Buhler & Holmes-Cerfon, 2009; Polzin & Ferrari, 2004). Regarding this process Polzin and Ferrari (2004) says "In contrast to fully developed turbulence, the internal wave field is inefficient at dispersing tracers. A single internal wave is nondispersive in the sense that tracer particles wind up at their original positions after a wave period, and thus experience no net displacement. Dispersion by internal waves appears only as a second-order Stokes drift effect, due to nonresonant wave-wave interactions." Consistent with this notion, several studies which examined wave fields' influence on tracer particle motion in inviscid regimes concluded that only the nonlinear, second-order corrections to the velocity field which arise from wave–wave interactions, play a significant role in setting the particle diffusivity (Buhler & Holmes-Cerfon, 2009; Bühler et al., 2013; Holmes-Cerfon et al., 2011; Sanderson & Okubo, 1988). Assuming that leading order wave effects make only a negligible contribution to tracer transport, these studies showed that the effective diffusivity scales with higher order powers of the wave amplitude.

Shear dispersion is another mechanism by which waves could induce a lateral diffusivity for tracers (Young et al., 1982), this mechanism needing diffusive effects to come in to play. Young et al. (1982) showed that the interaction of vertical diffusion and vertical shear of the wave field leads to an increased horizontal diffusion of the tracer field and this is identified as shear dispersion. Thus, it is the combined effect of internal wave vertical shear and the vertical diffusion that leads to the enhanced lateral mixing of the tracer field. Consequently, shear dispersion mechanism will be absent in the inviscid limit where there is no vertical diffusion. Additionally, studies point out that shear dispersion cannot account for the enhanced submesoscale diffusivity found in observations (J. Ledwell et al., 1993; J. R. Ledwell et al., 1998; Shcherbina et al., 2015). Shcherbina et al. (2015) for instance observed $\mathcal{O}(1)$ lateral diffusivity values for the tracer field at submesoscales, which is much higher than the estimates predicted based on shear dispersion.

As emphasized earlier, the above described secondary mechanisms involving waves and tracer stirring ignore the role of first order stirring by internal gravity waves, which could have an impact in wave-rich oceanic regions. In this study we explore stirring by internal waves using theoretical and numerical approaches. We study tracer dispersion using kinematic wave fields, constructed so as to avoid nonlinear wave interactions, and dynamic models that have nonlinear interactions. These collection of models allow us to explore tracer stirring by waves of different amplitudes across broad parameter regimes.

The plan of the paper is as follows: Section 2 presents theoretical and numerical analysis of tracer dispersion by a single wave, two waves, and three waves, Section 3 discusses numerical results on the dispersion of tracers by a spectrum of non-interacting waves, Section 4 presents results from dynamical models, and in Section 5 we conclude with a detailed summary and implications of our findings.

2. Tracer Dispersion by Discrete Waves

Much of the phenomenological mechanisms of tracer stirring in three dimensions can be captured by two dimensional models as well. We will therefore start with a passive tracer field θ being advected by an incompressible two dimensional flow $\boldsymbol{v} = (u, v)$, u and v being the x and y velocity components. The tracer advection equation is

$$\frac{\partial \theta}{\partial t} + \boldsymbol{v} \cdot \nabla \theta = 0. \tag{1}$$

In the above equation, θ and $\boldsymbol{v}$ depend on the position vector $\boldsymbol{x} = (x, y)$ and time t. The operator $\nabla = (\partial/\partial x, \partial/\partial y)$ is the two dimensional gradient operator. Since we consider an incompressible flow, we have $\nabla \cdot \boldsymbol{v} = 0$.

Equation 1 conserves tracer variance integrated over the whole domain $\mathcal{D}$ as

$$\frac{\mathrm{d}\Theta}{\mathrm{d}t} = 0, \quad \Theta(t) = \frac{1}{2}\int_{\mathcal{D}} \theta^2 \, \mathrm{d}\boldsymbol{x} \tag{2}$$

where Θ is the domain integrated or net tracer variance and θ^2 is the pointwise tracer variance.

For our kinematic experiments, which will be discussed in the subsequent sections, we obtain the velocity fields using a streamfunction formulation such that, by construction, the velocity fields satisfy the incompressibility condition. If the streamfunction is represented as $\psi(\boldsymbol{x}, t)$, then the velocity field $\boldsymbol{v} = (u, v) = \nabla^{\perp}\psi = (-\partial\psi/\partial y, \partial\psi/\partial x)$, where $\nabla^{\perp} = (-\partial/\partial y, \partial/\partial x)$ is the perpendicular gradient operator.

Oceanic waves fields are often composed of dominant discrete waves such as inertial waves, first baroclinic mode tides, etc., and their harmonics that stand out in a typical oceanic frequency spectra (M. Alford et al., 2016; Arbic, 2022; Polzin & Lvov, 2011; Nelson et al., 2020). Consequently, we will first look at tracer stirring by a few discrete waves, before focusing on a broad spectrum of waves.

2.1. Single Plane Wave

To obtain a single plane wave we set the streamfunction to be

$$\psi(\mathbf{x}, t) = \epsilon\left(e^{i(\boldsymbol{k}\cdot\boldsymbol{x} - \omega t + \phi)} + e^{-i(\boldsymbol{k}\cdot\boldsymbol{x} - \omega t + \phi)}\right) = 2\epsilon \cos(\boldsymbol{k}\cdot\boldsymbol{x} - \omega t + \phi), \tag{3}$$

where ϵ is a real number representing the wave amplitude and ϕ is the phase associated with the wave. Small amplitude waves will have $\epsilon \ll 1$ and waves with $\epsilon = \mathcal{O}(1)$ are what we will call order-one or finite amplitude waves. In Equation 3, $\boldsymbol{k} = (k_x, k_y)$ is the wavenumber vector along the propagation direction of the wave and ω is the wave frequency. This wave frequency can be any arbitrary function of the wavenumbers k_x and k_y. Here, we will present results for the dispersion relationship:

$$\omega^2 = 1 + k^2 \tag{4}$$

where $k = \sqrt{k_x^2 + k_y^2}$. This functional form for ω is inspired from the dispersion relation of hydrostatic Boussinesq internal waves, which in dimensional form reads: $\omega^2 = f^2 + N^2k^2/k_z^2$, with f being the inertial frequency, N the constant buoyancy frequency, and k_z the vertical wavenumber. When k_z is fixed, such as first baroclinic mode for tides or a high mode for near-inertial waves, ω depends on the horizontal wavenumber as $\omega^2 = f^2 + c^2k^2$, where $c = N/k_z$. This form is similar to Equation 4 if we set $f = c = 1$, following non-dimensionalization of variables. Furthermore, our choice in Equation 4 also mirrors the linear rotating shallow water (RSW) system where the inertia-gravity waves satisfy the dispersion relation in dimensional form as $\omega^2 = f^2 + gHk^2$, where g is the acceleration due to gravity and H is the mean layer thickness. This particular form also simplifies to Equation 4 if we choose $f = gH = 1$, moving to a non-dimensional form.

The velocity field corresponding to Equation 3 is

$$\boldsymbol{v} = \nabla^{\perp}\psi = \left(-\frac{\partial\psi}{\partial y}, \frac{\partial\psi}{\partial x}\right) = (2\epsilon k_y \sin(\boldsymbol{k}\cdot\boldsymbol{x} - \omega t + \phi),\ -2\epsilon k_x \sin(\boldsymbol{k}\cdot\boldsymbol{x} - \omega t + \phi)). \tag{5}$$

Using above velocity field in Equation 1 gives

$$\frac{\partial\theta}{\partial t} + 2\epsilon k_y \sin(\boldsymbol{k}\cdot\boldsymbol{x} - \omega t + \phi)\frac{\partial\theta}{\partial x} - 2\epsilon k_x \sin(\boldsymbol{k}\cdot\boldsymbol{x} - \omega t + \phi)\frac{\partial\theta}{\partial y} = 0. \tag{6}$$

Above equation can be solved analytically using the method of characteristics (MOC) for an arbitrary tracer initial condition $\theta_0(x,y)$ (see Appendix A for details) and the solution takes the form

$$\begin{aligned}\theta(\boldsymbol{x},t) = \theta_0\bigg(&x - \frac{2\epsilon k_y}{\omega}[\cos(\boldsymbol{k}\cdot\boldsymbol{x} - \omega t + \phi) - \cos(\boldsymbol{k}\cdot\boldsymbol{x} + \phi)],\\ &y + \frac{2\epsilon k_x}{\omega}[\cos(\boldsymbol{k}\cdot\boldsymbol{x} - \omega t + \phi) - \cos(\boldsymbol{k}\cdot\boldsymbol{x} + \phi)]\bigg).\end{aligned} \tag{7}$$

Notice that in Equation 7, time dependence enters only through the phase of the cosine terms, implying that the time-evolving tracer field will return exactly to its initial state, $\theta_0(x,y)$, whenever ωt is an integer multiple of 2π. This indicates that in a flow composed of a single plane wave, the tracer field is not stirred and mixed. Rather the tracer undergoes oscillations about its initial position. It is also evident from Equation 7 that, for a given $\boldsymbol{k}$, the wave amplitude ϵ influences only the extent of tracer field stretching. For small values of ϵ, the tracer field undergoes only slight stretching in x and y directions, resulting in a small maximum displacement before it returns to its initial state. As ϵ increases, this maximum excursion becomes larger. Nevertheless, the tracer field always recovers its original configuration, and the period of return is independent of the value of ϵ.

To illustrate above mentioned dynamics, we choose an example case where the wavenumber vector $\boldsymbol{k} = (1,0)$, $\phi = 0$, $\epsilon = 1$, and the frequency ω is computed from Equation 4. For the chosen $\boldsymbol{k}$, $\omega = \sqrt{2}$ which implies that the time period over which the tracer returns to its initial state is $\tau = \sqrt{2}\pi$. We used two different initializations for the tracer field, (a) a localized Gaussian blob, $\theta_0(x,y) = (1/2\sigma^2)\exp\left(\left(-(x-\pi)^2 - (y-\pi)^2\right)/(2\sigma^2)\right)$ with $\sigma = 0.4$ and (b) a broadly distributed sinusoidal structure, $\theta_0(x,y) = \sin x \cos y$.

In the first row of Figure 1, for the Gaussian blob initialization, we use the analytical solution Equation 7 to plot snapshots of the tracer field at different times. Notice that the tracer field undergoes some stretching and then returns to its initial state. In Figure 1c, observe that the tracer field resembles the initial state showed in Figure 1a, which is obtained at a time $t = 40 \approx 9\tau$. In the case of sinusoidal initialization as well (third row of Figure 1), the large scale tracer field structures only get stretched with time and retain its initial structure after the same period of time as in the Gaussian case. These results highlight that irrespective of the tracer initialization, a single plane wave only oscillates the tracer field about its initial state. In order to verify our analytical findings, we also performed numerical simulations of Equation 6 and obtained the solutions. Details of our numerical setup can be found in Appendix E. Numerically obtained time snapshots of tracer field for Gaussian blob and sinusoidal initializations are shown in the second and fourth rows of Figure 1, respectively, and are found to be in excellent agreement with the analytical results.

Changing the wavenumber vector $\boldsymbol{k}$ will lead to variations in the stretching directions and period of return of the tracer field, as ω depends on the components of the wave vectors. Barring these details, the qualitative insights from above illustrations carry over to other configurations with a single plane wave stirring: irreversible tracer stirring and dispersion does not take place with one plane wave. We will next add one more wave to see how stirring changes.

2.2. Two Plane Waves

We construct a flow having two plane waves by using the streamfunction

$$\psi(\boldsymbol{x},t) = 2\epsilon_1\cos\left(\boldsymbol{k}_1\cdot\boldsymbol{x} - \omega_1 t + \phi_1\right) + 2\epsilon_2\cos\left(\boldsymbol{k}_2\cdot\boldsymbol{x} - \omega_2 t + \phi_2\right) \tag{8}$$

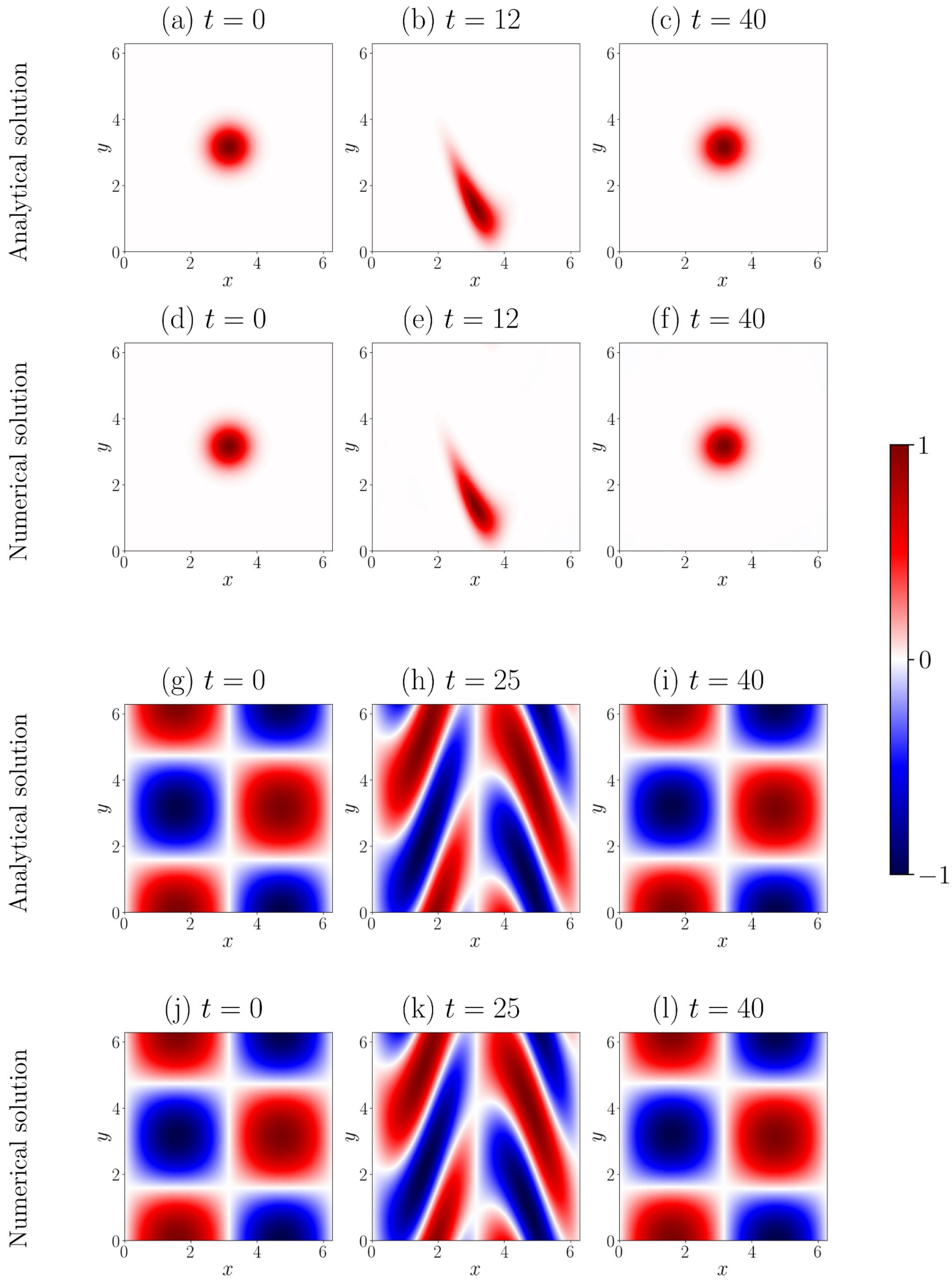

Figure 1. Temporal evolution of tracer field advected by a single wave. Comparison of analytical and numerical solutions for two different initializations: (i) Gaussian blob (top two rows) and (ii) sinusoidal (bottom two rows).

where ϵ_1 and ϵ_2 determine the amplitude of the two waves. Propagation directions of the waves are determined by the wavenumber vectors $\boldsymbol{k}_1$ and $\boldsymbol{k}_2$, and the phases are denoted by ϕ_1 and ϕ_2. The frequencies of the two waves are ω_1 and ω_2, and their relationship with the wavenumber vectors is given by the same dispersion relation in Equation 4. From Equation 8 the velocity field is

$$\boldsymbol{v} = \nabla^{\perp}\psi = \left(2\epsilon_1 k_{1_y} \sin\left(\boldsymbol{k}_1 \cdot \boldsymbol{x} - \omega_1 t + \phi_1\right) + 2\epsilon_2 k_{2_y} \sin\left(\boldsymbol{k}_2 \cdot \boldsymbol{x} - \omega_2 t + \phi_2\right),\right.$$
$$\left. -2\epsilon_1 k_{1_x} \sin\left(\boldsymbol{k}_1 \cdot \boldsymbol{x} - \omega_1 t + \phi_1\right) - 2\epsilon_2 k_{2_x} \sin\left(\boldsymbol{k}_2 \cdot \boldsymbol{x} - \omega_2 t + \phi_2\right)\right) \tag{9}$$

and using above, Equation 1 becomes

$$\frac{\partial\theta}{\partial t} + \left(2\epsilon_1 k_{1_y} \sin\left(\boldsymbol{k}_1 \cdot \boldsymbol{x} - \omega_1 t + \phi_1\right) + 2\epsilon_2 k_{2_y} \sin\left(\boldsymbol{k}_2 \cdot \boldsymbol{x} - \omega_2 t + \phi_2\right)\right)\frac{\partial\theta}{\partial x}$$
$$-\left(2\epsilon_1 k_{1_x} \sin\left(\boldsymbol{k}_1 \cdot \boldsymbol{x} - \omega_1 t + \phi_1\right) + 2\epsilon_2 k_{2_x} \sin\left(\boldsymbol{k}_2 \cdot \boldsymbol{x} - \omega_2 t + \phi_2\right)\right)\frac{\partial\theta}{\partial y} = 0. \tag{10}$$

Unlike Equation 6, it is challenging to obtain a closed form analytical solution of Equation 10 using MOC. To make progress, we perform variable transformations of the form

$$T = t \quad ; \quad X = \boldsymbol{k}_1 \cdot \boldsymbol{x} - \omega_1 t + \phi_1 \quad ; \quad Y = \boldsymbol{k}_2 \cdot \boldsymbol{x} - \omega_2 t + \phi_2 \tag{11}$$

and rewrite Equation 10 in terms of the transformed variables to get

$$\frac{\partial\theta}{\partial T} + (2\epsilon_2 K \sin Y - \omega_1)\frac{\partial\theta}{\partial X} + (-2\epsilon_1 K \sin X - \omega_2)\frac{\partial\theta}{\partial Y} = 0 \tag{12}$$

with $K = k_{1_x}k_{2_y} - k_{2_x}k_{1_y}$. At this stage, we can apply MOC for the above equation and show that there exists a conserved quantity G such that

$$G(X, Y) = 2K(\epsilon_1 \cos X + \epsilon_2 \cos Y) + \omega_1 Y - \omega_2 X = C \tag{13}$$

where C is a constant (see Appendix B for details). In a plane defined by the transformed coordinates X and Y, the above equation provides a family of curves which does not vary with time. Even though G is stationary in the (X, Y) space, the G field in (x, y) plane exhibits a time-dependent drift which arises from the transformation relations given in Equation 11. To understand the significance of these G curves, we rewrite Equation 12 using G as

$$\frac{\partial\theta}{\partial T} + \left(\widetilde{\nabla}^{\perp} G\right) \cdot \widetilde{\nabla}\theta = 0. \tag{14}$$

where $\widetilde{\nabla} = (\partial/\partial X, \partial/\partial Y)$ and $\widetilde{\nabla}^{\perp} = (-\partial/\partial Y, \partial/\partial X)$. The above equation implies that the tracer field does not get stretched along the isolines of G. To see this explicitly, consider a tracer arrangement of the form $\theta = \Gamma(G)$, Γ being any arbitrary function of G. This gives $\widetilde{\nabla}\theta = \Gamma'(G)\widetilde{\nabla}G$, where prime denotes differentiation. Substituting this in Equation 14 leads to the vanishing of the second term and the tracer does not evolve with time. Therefore, a tracer field aligned along the isolines of G preserves its form. The form of Equation 14 also implies that maximum stretching of the tracer field takes place orthogonal to the isolines of G.

Now, an arbitrary initialization of the tracer field need not have the special form $\theta = \Gamma(G)$ and therefore such a tracer field will get stretched and stirred until the tracer aligns along isolines of G. Once it aligns with the isolines of G, stirring stops, although the tracer will not return to the initial arbitrary state. This process leads to irreversible stirring of the tracer, from an arbitrary initial structure to a form where it aligns with the isolines of G. Two plane waves therefore can stir and disperse a tracer field, unlike the single plane wave case discussed earlier where the tracer periodically returns to the initial state.

To see above dynamics, we numerically integrated Equation 10 by using the same two tracer initializations as in the single plane wave case (see Appendix E for more details on the numerics). Here we will show an example case where velocity fields were generated using $\boldsymbol{k}_1 = (1, 0)$ and $\boldsymbol{k}_2 = (0, 1)$, resulting in frequencies $\omega_1 = \omega_2 = \sqrt{2}$ (from Equation 4). We chose amplitudes $\epsilon_1 = \epsilon_2 \lesssim 1$, with the phases being $\phi_1 = \phi_2 = 0$.

In Figure 2, we show snapshots of the tracer field for the same two different initializations used in the single plane wave case, with $\epsilon_1 = \epsilon_2 = 1$. While the first row shows the tracer field structures obtained at different times for

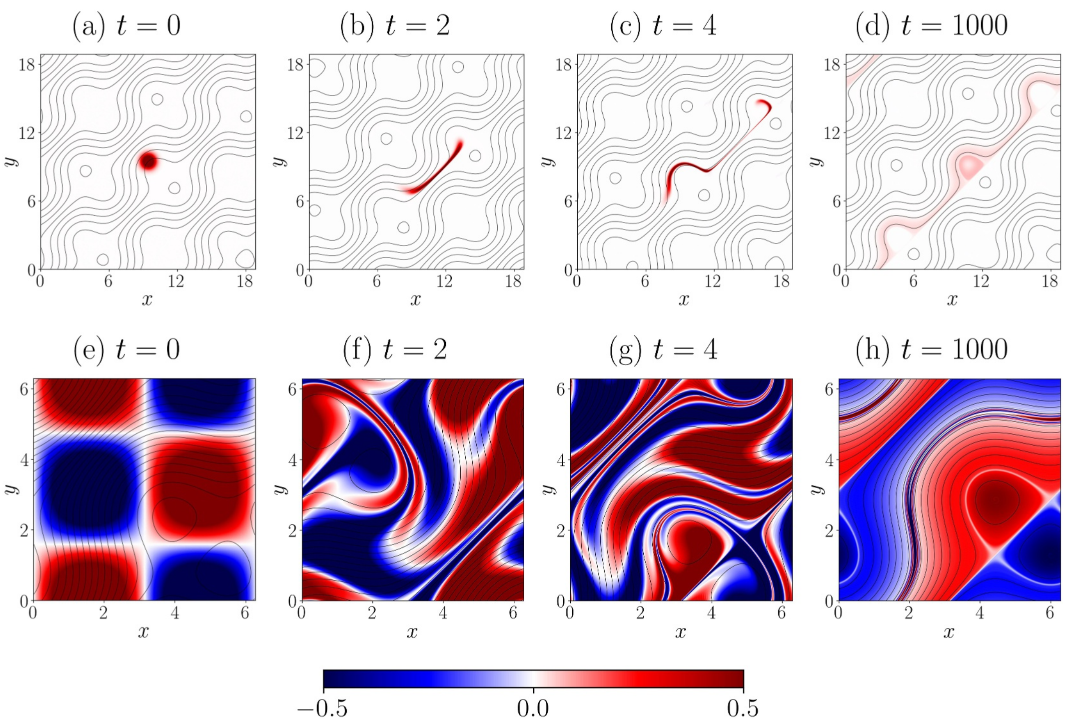

Figure 2. Snapshots of tracer field structures at different times for the Gaussian blob (first row) and the sinusoidal (second row) initializations. Black lines indicate the contours corresponding to $G(x, y, t) = C$ which can be obtained from Equation 13 by using Equation 11.

the Gaussian blob initialization, second row corresponds to tracer structures for the sinusoidal initialization at the same times as in the first row. Thin black lines represent isolines of curves defined by G. Notice that in the case of Gaussian initialization (first row of Figure 2), as we move from left to right the Gaussian blob experiences stretching and eventually aligns along the contours represented by the thin black lines (Figure 2d). The smallest scales of the tracer gets diffused in the process, leading to fading color of the tracer with time, as seen in the figure. Similar observations are seen in the case of sinusoidal initialization as well (second row of Figure 2). Stretching and rearrangement of the tracer field can be observed at early times (Figures 2f and 2g) and the tracer field eventually gets aligned along the isolines of G (Figure 2h). Here as well, the formation of thin filaments is evident, and this leads to eventual tracer mixing. These observations highlight that two plane waves can stir, disperse, and induce mixing of the tracer field.

To quantify the observed mixing of the tracer field, we computed the temporal evolution of domain integrated tracer variance Θ, which is defined in Equation 2. In Figure 3a, we show the variation of normalized domain integrated tracer variance with time for the Gaussian and sinusoidal initializations of the tracer field. The normalization is performed by using the domain integrated tracer variance value at $t = 0$, represented as Θ_0. For both cases (solid lines), we observe an initial decay of Θ, but eventually tracer variance reaches a saturated state with no further decay. This is consistent with our observation from Figure 2 where we saw the alignment of the tracer field along the isolines of G. A low saturation value for the tracer variance is observed in the Gaussian case (red line) because, the tracer field is already initialized at comparatively smaller scale than that of the sinusoidal case and hence dissipation effects act on the Gaussian blob case more effectively than the sinusoidal case.

The above results were for $\epsilon_1 = \epsilon_2 = 1$. We also performed simulations with small wave amplitudes, and observed weakening of tracer mixing. In the sinusoidal case nearly 70% of the tracer variance decays by $t = 1000$, which is about 230 wave periods, when the wave amplitudes are $\epsilon_1 = \epsilon_2 = 1$ (solid black line in Figure 3a). In contrast, when the amplitudes are reduced to $\epsilon_1 = \epsilon_2 = 0.1$, the tracer variance remains almost unchanged (dashed line) in the same interval of time. Even by $t = 10000$, which is around 2,300 wave periods, only about 40% of the variance has decayed (see inset of the figure), illustrating the substantial reduction in the

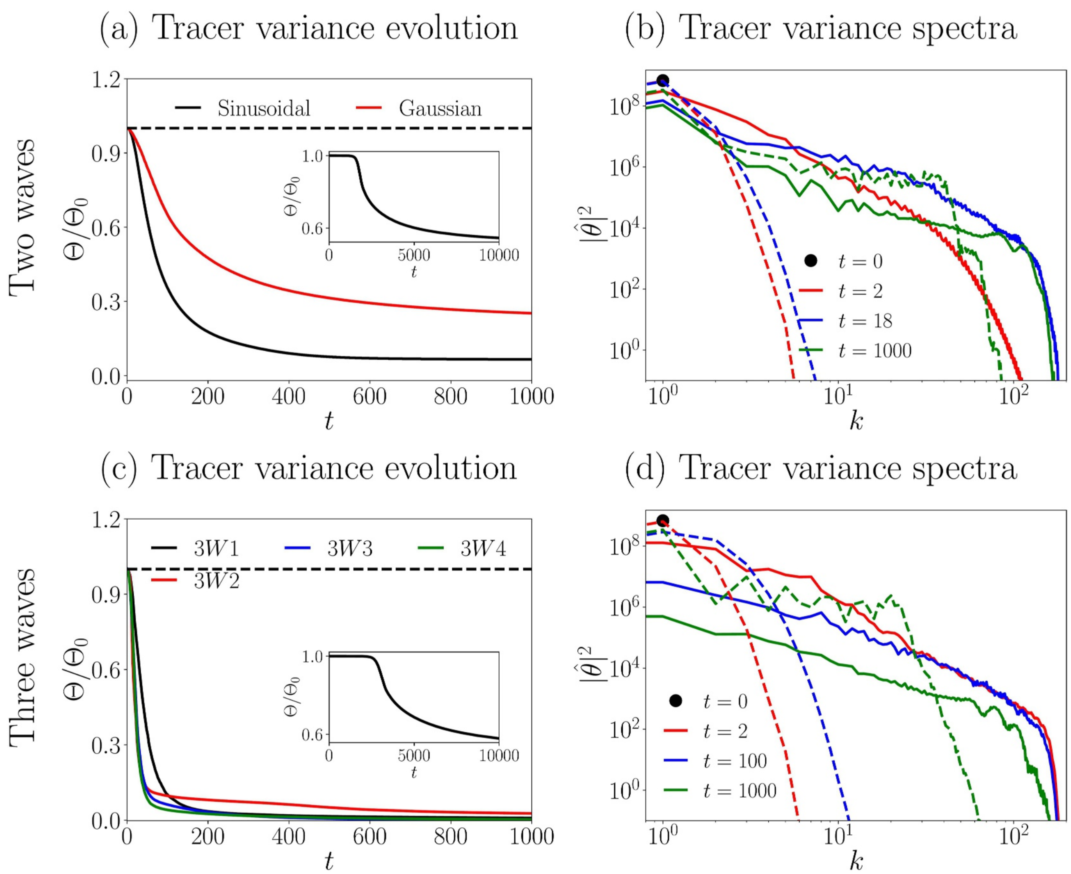

Figure 3. (a) Temporal evolution of normalized net tracer variance in the case of two waves with $\epsilon_1 = \epsilon_2 = 1$ is shown with solid lines. The dashed line shows the tracer variance evolution when $\epsilon_1 = \epsilon_2 = 0.1$. Inset: Temporal evolution of tracer variance for the sinusoidal case with $\epsilon_1 = \epsilon_2 = 0.1$ is shown for a long interval of time. (b) Tracer variance spectra at different times for the two-wave simulations. Solid lines represent $\epsilon_1 = \epsilon_2 = 1$ and dashed lines correspond to $\epsilon_1 = \epsilon_2 = 0.1$. (c) Evolution of normalized net tracer variance for the different cases of three waves for $\epsilon_1 = \epsilon_2 = \epsilon_3 = 1$ is shown with colored solid lines. The dashed black line shows the temporal evolution of tracer variance in the $3W_1$ case with $\epsilon_1 = \epsilon_2 = \epsilon_3 = 0.1$ up to $t = 1000$. Inset of the figure shows this case for $t = 10000$. (d) The evolution of tracer variance spectra with time for $3W_1$ with $\epsilon_1 = \epsilon_2 = \epsilon_3 = 1$ is shown with solid lines and $\epsilon_1 = \epsilon_2 = \epsilon_3 = 0.1$ is shown with dashed lines.

mixing of tracer field when the wave amplitudes are decreased by an order of magnitude. Therefore, tracer dispersion is stronger for higher amplitude waves.

To see the distribution of tracer variance across spatial scales, we look at the tracer variance spectra, $|\hat{\theta}|^2$, which is computed by performing a two dimensional Fourier transform of the tracer field and then computing the tracer variance as a function of the wavenumber k. Throughout this paper, the overhat symbol is used to represent Fourier transformed variables. In Figure 3b, we show the tracer variance spectra at different times for the sinusoidal case. At $t = 0$, all the tracer variance is concentrated at $k = 1$ because of our sinusoidal initialization. It is to be noted that, according to our sinusoidal initialization, the tracer variance should have been concentrated at $k = \sqrt{2}$ at $t = 0$. However, because of the spectral binning implemented (see Appendix D), we observe tracer variance value concentrated at $k = 1$. With time, we observe the evolution of the spectrum toward higher wavenumbers, indicating the transfer of tracer variance from large to small scales. The tracer content at small wavenumbers decrease and we observe tracer variance reaching large wavenumbers where it gets dissipated. When $\epsilon_1 = \epsilon_2 = 0.1$ (see dashed lines), the evolution of spectrum is very slow and we do not see a well developed spectrum even by $t = 1000$. This once again highlights the inefficiency of small amplitude waves in dispersing the tracer field. Similar conclusions were obtained from the spectra of Gaussian blob case as well (not shown here in the interest of space). These observations allow us to conclude that a minimum of two waves, having $\mathcal{O}(1)$ values for the amplitudes ϵ_1 and ϵ_2, is sufficient enough to induce stirring and mixing of a passive tracer field.

Apart from analyzing the impact of varying wave amplitudes, we also explored how different configurations of wave propagation directions affect tracer dispersion. Interestingly, there is one special case of two plane waves where tracer dispersion does not happen. This is for two collinear waves having equal wavenumber vector magnitude. Such a flow, where the wavenumber vectors of the two waves lie on a straight line is similar to one wave case and the tracer field oscillates about its initial state. For example, consider two waves with $\boldsymbol{k_1} = (1,0)$ and $\boldsymbol{k_2} = (-1,0)$. The corresponding tracer equation can be solved using MOC for this special case to obtain (see Appendix B for details)

$$\begin{aligned}\theta(\boldsymbol{x},t) = \theta_0\bigg(x, y + \frac{2\epsilon_1}{\omega_1}\left[\cos\left(x-\omega_1 t+\phi_1\right) - \cos\left(x+\phi_1\right)\right] \\ -\frac{2\epsilon_2}{\omega_2}\left[\cos\left(x+\omega_2 t+\phi_2\right) - \cos\left(x+\phi_2\right)\right]\bigg)\end{aligned} \tag{15}$$

for the initial condition $\theta_0(x,y)$. Because the chosen wavenumber vectors have the same magnitude, here $\omega_1 = \omega_2 = \sqrt{2}$. This implies that irrespective of the amplitudes ϵ_1 and ϵ_2, the tracer field returns to its initial state over the period of time $\tau = \sqrt{2}\pi$. This behavior is similar to the one wave case and indicate the inefficiency of the flow in dispersing the tracer field. However, if $|\boldsymbol{k_1}| \neq |\boldsymbol{k_2}|$, then $\omega_1 \neq \omega_2$. In this case the tracer field can undergo irreversible stretching which eventually leads to tracer mixing.

Two collinear waves with same wavenumber vector magnitude therefore cannot stir tracers irreversibly, while changing the alignment of waves starts stirring the tracers. Increasing the angle between the wavenumber vector leads to more efficient stirring, with maximum stirring and mixing of the tracer field being achieved when the two plane waves propagate in directions perpendicular to each other.

As seen in this subsection, adding an extra wave to the single plane wave case led to irreversible stirring. Nevertheless, while above analysis shows that two arbitrary plane waves can stir and disperse tracers, the stirring is in some sense limited and saturates once the tracer aligns with the isolines of G curves. We will now add one more wave to the system and see how stirring changes.

2.3. Three Plane Waves

Adding one more plane wave into Equation 8 gives us a three wave system:

$$\psi(\boldsymbol{x},t) = 2\epsilon_1\cos\left(\boldsymbol{k}_1\cdot\boldsymbol{x} - \omega_1 t + \phi_1\right) + 2\epsilon_2\cos\left(\boldsymbol{k}_2\cdot\boldsymbol{x} - \omega_2 t + \phi_2\right) + 2\epsilon_3\cos\left(\boldsymbol{k}_3\cdot\boldsymbol{x} - \omega_3 t + \phi_3\right) \tag{16}$$

where $\epsilon_3, \boldsymbol{k_3}, \omega_3$, and ϕ_3 correspond to the amplitude, wavenumber vector, frequency, and phase of the third wave, respectively. Proceeding in the same way as in the previous section, we can compute the velocity field and substitute in Equation 1 to get the evolution equation for the tracer field.

For the three waves system we did not find anything similar to the G contours observed in the two waves system, and the tracer field got stirred and dispersed continuously over time. Four cases selected from an exhaustive set of numerical simulations involving different three wave systems are:

- $3W_1: \boldsymbol{k_1} = \hat{\boldsymbol{y}}, \boldsymbol{k_2} = \hat{\boldsymbol{x}}, \boldsymbol{k_3} = \hat{\boldsymbol{x}} + \hat{\boldsymbol{y}}$
- $3W_2: \boldsymbol{k_1} = \hat{\boldsymbol{y}}, \boldsymbol{k_2} = \hat{\boldsymbol{x}} + \hat{\boldsymbol{y}}, \boldsymbol{k_3} = -\hat{\boldsymbol{x}} - \hat{\boldsymbol{y}}$
- $3W_3: \boldsymbol{k_1} = \hat{\boldsymbol{y}}, \boldsymbol{k_2} = \hat{\boldsymbol{x}} + \hat{\boldsymbol{y}}, \boldsymbol{k_3} = \hat{\boldsymbol{x}} - \hat{\boldsymbol{y}}$
- $3W_4: \boldsymbol{k_1} = \hat{\boldsymbol{y}}, \boldsymbol{k_2} = \hat{\boldsymbol{x}}, \boldsymbol{k_3} = \hat{\boldsymbol{x}} + 2\hat{\boldsymbol{y}}$

As in the two plane waves' case, we choose equal wave amplitudes $\epsilon_1 = \epsilon_2 = \epsilon_3 \lesssim 1$, and Equation 4 for the dispersion relation. Other numerical details are in Appendix E.

Figure 3c presents the time evolution of the normalized domain-integrated tracer variance for all four cases mentioned above. Unlike the two-wave scenario, all three-wave cases exhibit a rapid decay of net tracer variance toward zero. This behavior suggests that the downscale transfer of tracer variance to smaller, dissipation-dominated scales is more efficient in flows containing three plane waves than in those with only two. In the inset, we show the temporal evolution of tracer variance when $\epsilon_1 = \epsilon_2 = \epsilon_3 = 0.1$ for the $3W_1$ case. When $\epsilon_1 = \epsilon_2 = \epsilon_3 = 1$ (black line in the main figure panel), the tracer variance almost completely decayed by $t = 1000$, which is about 230 wave periods, wave period being based on the slowest evolving wave. However, the tracer variance did not show any variation in the case where $\epsilon_1 = \epsilon_2 = \epsilon_3 = 0.1$ over the same interval of time (dashed black line) and only dissipated about 40% by $t = 10000$ (see inset of figure panel), which is about 2,300 wave periods. This observation once again confirms that strong amplitude waves can enhance tracer mixing.

In Figure 3d we show the temporal evolution of the tracer variance spectra for the $3W_1$ case with $\epsilon_1 = \epsilon_2 = \epsilon_3 = 1$ as solid lines. As in the two plane waves' case, the tracer variance spreads across a wide range of wavenumbers with time, indicating spectral development. By $t = 1000$, the tracer variance spectra decreases by nearly two orders of magnitude in the three-wave case, significantly higher than the drop in the two-wave case. Looking at the dashed lines, which represent the case with $\epsilon_1 = \epsilon_2 = \epsilon_3 = 0.1$, we note the delay in the development of tracer variance spectra, further pointing out the inefficiency of the flow with low amplitude waves in the stirring and mixing of the tracer field. Similar evolution of the tracer variance spectra is observed in the $3W_2$, $3W_3$, and $3W_4$ cases (shown in Appendix C), although the magnitude of tracer variance decay differs among the cases.

Motivated by the intensified tracer stirring by three finite amplitude plane waves, we extend our numerical experiments to flows containing a larger number of waves with different magnitude for the wave amplitudes and investigate the resulting tracer dynamics.

3. Tracer Dispersion by a Spectrum of Non-Interacting Waves

The above findings reveal that a few discrete waves can irreversibly stir and mix tracers. Oceanic flows, in addition to dominant discrete waves with specific frequencies, also contain broad band spectrum of waves, such as the Garret-Munk spectrum (Garrett & Munk, 1979). To mimic such a spectrum of waves, we will continue the above construction of waves to make a broader spectrum. These broadband wave fields will be kinematic, implying that they do not have nonlinear interactions and higher order effects, allowing us to focus on the features of the leading order wave field.

As in the previous cases, we construct incompressible velocity fields using the streamfunction formulation. The streamfunction for a spectrum of waves take the form

$$\psi(\boldsymbol{x},t) = \epsilon \sum_{|\boldsymbol{k}_n|>0}^{|\boldsymbol{k}|} a_{\boldsymbol{k}_n} \cos(\boldsymbol{k}_n \cdot \boldsymbol{x} - \omega_{k_n} t + \phi(\boldsymbol{k}_n)) \tag{17}$$

where $\boldsymbol{k_n}$ denotes the wavenumber vector, ω_{k_n} is the wave frequency which is related to the wavenumber vector magnitude as in Equation 4, and $\phi(\boldsymbol{k_n})$ is the phase associated with the wave. Here, the overall magnitude of the wave amplitudes are controlled by two parameters: the scaling parameter ϵ which determines the global strength of the velocity field and the spectral amplitude $a_{\boldsymbol{k}_n}$, which specifies the relative weight of each mode. With the above choice of the streamfunction, we generate flows having different number of wave modes. For instance, if $|\boldsymbol{k}| = 1$, we introduce waves at all wavenumbers whose magnitude is greater than 0 and less than or equal to 1. Thus, in this context we will have four plane waves with $\boldsymbol{k_1} = (1,0)$, $\boldsymbol{k_2} = (-1,0)$, $\boldsymbol{k_3} = (0,1)$, and $\boldsymbol{k_4} = (0, -1)$. We represent this choice as Case 1 and the simulations with $|\boldsymbol{k}| = 10$ and $|\boldsymbol{k}| = 128$ are identified as Case 2 and Case 3, respectively. We chose wave amplitudes $a_{\boldsymbol{k}_n}$ to get different power laws for the wave spectra, such as $-5/3$, -2, -3, etc. We also experimented with different wave phases $\phi(\boldsymbol{k_n})$. These different choices led to qualitative similar results and here we will present results for $-5/3$ slope wave spectrum with $\phi(\boldsymbol{k_n}) = 0$. For this configuration, wave spectra for Case 2 and Case 3 are shown in Figure 4a, where $\epsilon = 1$. Case 1 does not have a spectrum as the wave fields are initialized only at $k = 1$ mode.

Having obtained the flow velocity fields from Equation 17 for the above discussed three cases, we advect the tracer field using

$$\frac{\partial \theta}{\partial t} + \boldsymbol{v} \cdot \nabla \theta = F - D \tag{18}$$

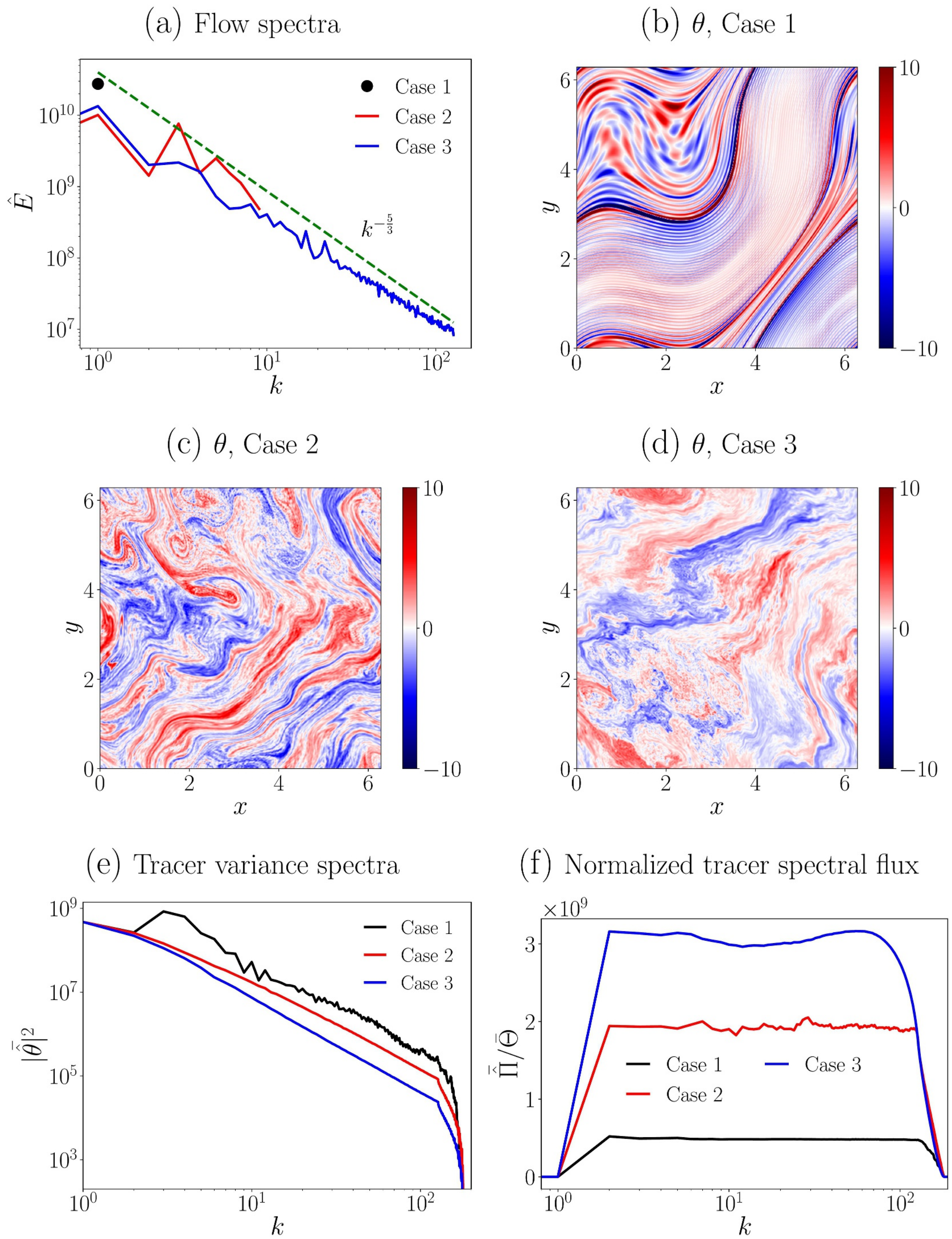

Figure 4. Flow spectra obtained for the three cases are shown in panel (a). Tracer field structures at a particular instant of time for Case 1 (b), Case 2 (c), and Case 3 (d) are shown. Time-averaged tracer variance spectra, and normalized tracer spectral flux are shown in (e) and (f) respectively.

where F is the forcing and D is the dissipation term. Recall that in our previous experiments the tracer field decayed with time. The forcing term F above supplies tracer variance at large scales, thereby allowing the tracer to attain an equilibrium state. This will in turn allows us to evaluate tracer spectral flux, which will indicate the rate at which tracer variance is cascaded to small scales. Appendix E provides details on the numerical setup, dissipation term, and the implementation of tracer forcing.

In Figures 4b–4d, we show the steady state tracer field structures in the three cases with $\epsilon = 1$. For Case 1 (Figure 4b), we observe stretching and formation of small scales. Compared to the case of two waves (Figure 2h), we see the formation of more small scale structures in this case, which is expected because Case 1 has four plane waves, as mentioned earlier. Visually, we find the formation of much more small scale structures in Case 2 and Case 3, compared to Case 1 (Figures 4c and 4d). In contrast to the tracer patterns produced by two plane waves, all three cases here exhibit pronounced small-scale features, highlighting increased stirring and mixing of the tracers.

In Figure 4e, we plot the time-averaged tracer variance spectra, $|\overline{\hat{\theta}}|^2$, for the three cases. In contrast to Figures 3b and 3d, here, all cases exhibit the same tracer variance at $k = 1$ due to the applied tracer forcing. Although the forcing is implemented at $k = \sqrt{2}$, identical values appear at $k = 1$ in the plot because of the usage of spectral binning (see Appendix D). Increased stirring depletes tracer variance at a scale faster, leading to lower tracer concentration at that scale. This leads to the steepening of tracer variance spectrum as we go from Case 1 to Case 3.

For quantifying tracer stirring in these flows with different number of waves, we next compute tracer spectral flux which measures the amount of tracer variance transferred across different scales in the flow. This is done by first performing a two dimensional Fourier transform of Equation 18, after omitting the dissipation and forcing terms, to get

$$\frac{\partial \hat{\theta}}{\partial t} + \widehat{\nabla \cdot (\theta \boldsymbol{v})} = 0. \tag{19}$$

Forcing and dissipation terms are omitted because we are interested in the transfer of tracer variance across the inviscid inertial range, far from the dissipation and forcing scales. Multiplying Equation 19 by the complex conjugate of $\hat{\theta}$ and taking the real part of that equation gives the evolution equation of tracer variance at a particular wavenumber k. We then perform summation over a band of wavenumbers $[k, k_{\max}]$ such that

$$\frac{\mathrm{d}}{\mathrm{d}t} \sum_{q=k_{\max}}^{k} |\hat{\theta}(q,t)|^2 = \hat{\Pi}(k,t) \tag{20}$$

where the left hand side term denotes the rate of change of tracer variance in $[k, k_{\max}]$ and $\hat{\Pi}(k,t)$ is the spectral flux of tracer variance, which represents the transfer rate of tracer variance into or from the wavenumber band. Positive value of $\hat{\Pi}(k,t)$ suggests transfer into the wavenumber band, that is, a forward cascade of tracer variance.

Figure 4f shows the time-averaged tracer spectral flux, denoted as $\overline{\hat{\Pi}}$, which is normalized by time-averaged domain integrated tracer variance, $\overline{\Theta}$. This normalization is used because in each of the three cases Θ saturated at different levels. Note from the figure that in all the cases we obtain positive values for $\overline{\hat{\Pi}}$ in the inertial range, indicating downscale transfer of tracer variance from large to small scales. It is interesting to observe a monotonic increase in the value of $\overline{\hat{\Pi}}$ as we move from Case 1 to Case 3, signaling the enhancement of tracer cascade to small scales with increase in number of waves or broadening of the wave spectrum. Notice that the increase in flux from Case 1 to 2 is higher than the increase in flux from Case 2 to 3. This is because while increasing the number of wave modes we are still preserving the $-5/3$ power law for the flow spectrum (Figure 4a). Larger modes have less energy and therefore their contribution to stirring decreases with increase in mode number.

We have seen the enhancement in tracer stirring with increase in the number of waves in the flow. Now, we look at the impact of wave field strength, ϵ, on tracer stirring. For this, in each of the above discussed cases we vary the parameter ϵ between 0 and 1, and then advect the tracer field with the obtained velocity field. After the tracer field achieves a steady state, we compute and plot the normalized time-averaged tracer spectral flux, as shown in Figure 5. Irrespective of the number of waves, in each case, we observe highest values of normalized time-averaged tracer flux when $\epsilon = 1$ and the values monotonically decrease with decrease in ϵ. For example, normalized time-averaged tracer spectral flux values in Case 3 for $\epsilon = 1$ is about 1000 times higher than the case with $\epsilon = 0.1$. Decreasing the strength of waves therefore weakens stirring and mixing of tracers, this behavior being similar to what we saw earlier with a few discrete waves.

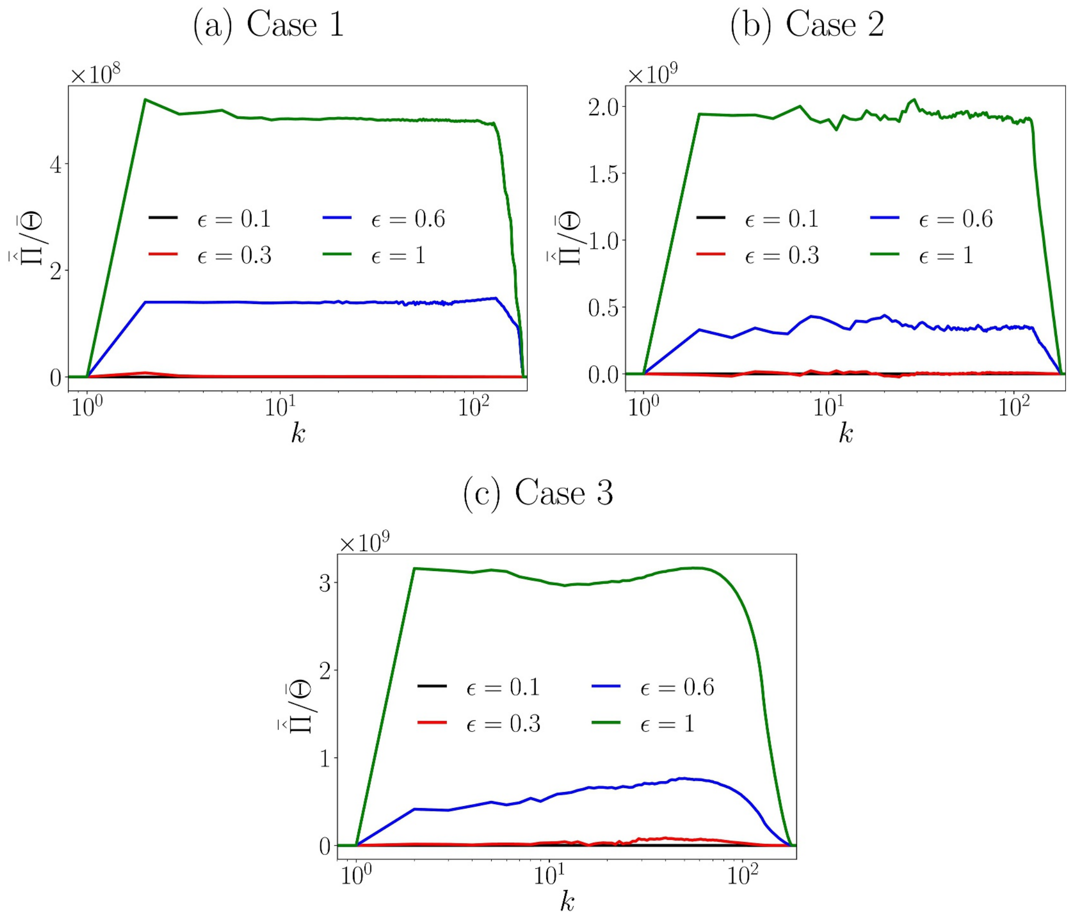

Figure 5. Normalized time-averaged tracer spectral flux comparison for different values of ϵ in Case 1 (a), Case 2 (b), and Case 3 (c).

The analytical and numerical observations so far using kinematic velocity fields revealed that linear waves are capable of dispersing tracers. Even though a single wave is inefficient in stirring and mixing tracers, two or more waves can disperse a passive tracer field and mix it up. We will next explore tracer stirring by dynamic model-generated waves.

4. Tracer Dispersion by Dynamically Interacting Waves

Up to this point, we examined tracer dispersion using kinematic wave models, where the flow was prescribed as a set of non-interacting waves. Such models isolate the leading order linear wave effects by construction and exclude any nonlinear interactions between waves. In this section, we turn to dynamic models that are widely used in oceanography. Using the RSW and Boussinesq equations, we generate wave-dominated flows in which the velocity fields evolve according to fully nonlinear equations. These dynamics include second order wave effects and hence represent a more realistic setting of an oceanic flow. We begin with the RSW model in the following subsection.

4.1. Rotating Shallow Water Equations

RSW is a model that captures the evolution of a thin layer of rotating fluid in hydrostatic balance (Salmon, 1978; Vallis, 2006). Both inertia-gravity waves and geostrophically balanced components exist in the dynamics of this model. Furthermore, wave-wave interactions and wave-vortex interactions can take place in this setting, with wave breaking at small scales leading to shock formation (J. Thomas et al., 2024; Zeitlin, 2018). We used the RSW model to construct wave-dominated flows and then advected a tracer field within this wavy flow. The equations and numerical details are provided in Appendix E.

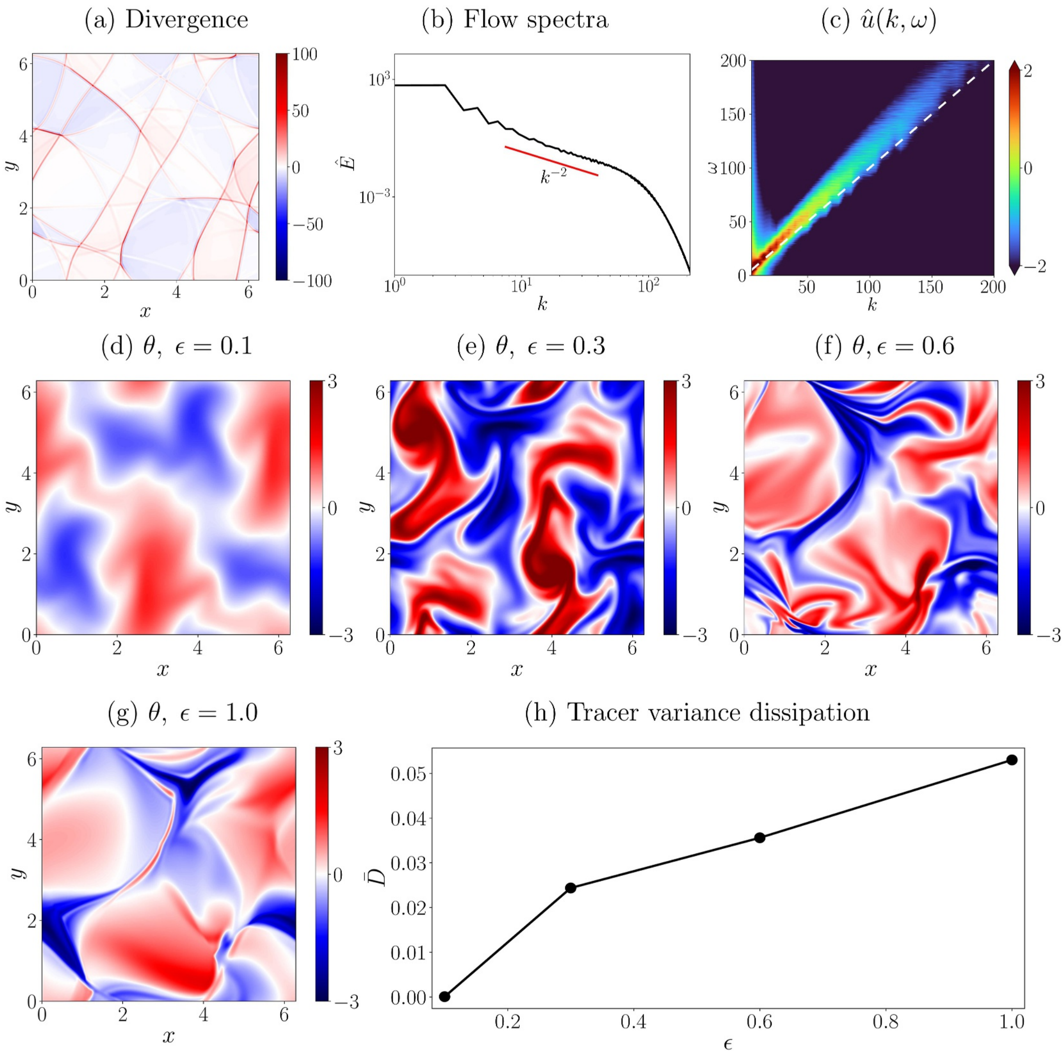

Figure 6. (a) Negative flow divergence exhibiting shocks is shown. (b) Energy spectrum for $\epsilon = 1$ case of the flow is shown with the red line representing k^{-2} line for reference. (c) Horizontal component of the velocity field is plotted in the frequency-wavenumber space with the white dashed line being the dispersion curve. Tracer field structures at a particular instant of time for different values of ϵ are shown in panels (d–g). (h) Time-averaged tracer variance dissipation is plotted as a function of ϵ.

Figure 6a shows the negative flow divergence, $-\nabla \cdot \boldsymbol{v}$, from the RSW model. Notice the strong localized peaks in divergence, these indicating shocks formed by wave breaking at small scales. The spatial structure of this field is similar to that discussed in J. Thomas et al. (2024). This flow has an energy spectrum with a -2 power law, as shown in Figure 6b. The frequency-wavenumber spectrum of the flow is shown in Figure 6c, with the dispersion curve being highlighted with the dashed white line. Notice the spread across the dispersion curve, indicating the nonlinear broadening of waves due to wave-wave interactions. This is a feature of waves generated from nonlinearly interacting dynamic models when compared to the kinematic models seen earlier. In the kinematic models the wave field is perfectly aligned along the dispersion curve with no spread across it.

Once the flow reached a steady state we integrated the tracer Equation 18 in forced-dissipative setting. To introduce a wave amplitude factor, we scaled the velocity obtained from RSW by ϵ, where $0 < \epsilon < 1$, and then used this scaled velocity for tracer advection. Thus, here as well, ϵ represents the magnitude of the wave amplitude, as in the previous cases. This procedure allows us to systematically control the wave strength while keeping the underlying flow structure fixed.

In Figures 6d–6g we present tracer field snapshots for $\epsilon = 0.1$, 0.3, 0.6, and 1.0. Notice that we see increased small scale features in the tracer field with increasing ϵ. Figure 6h shows the tracer dissipation as a function of ϵ.

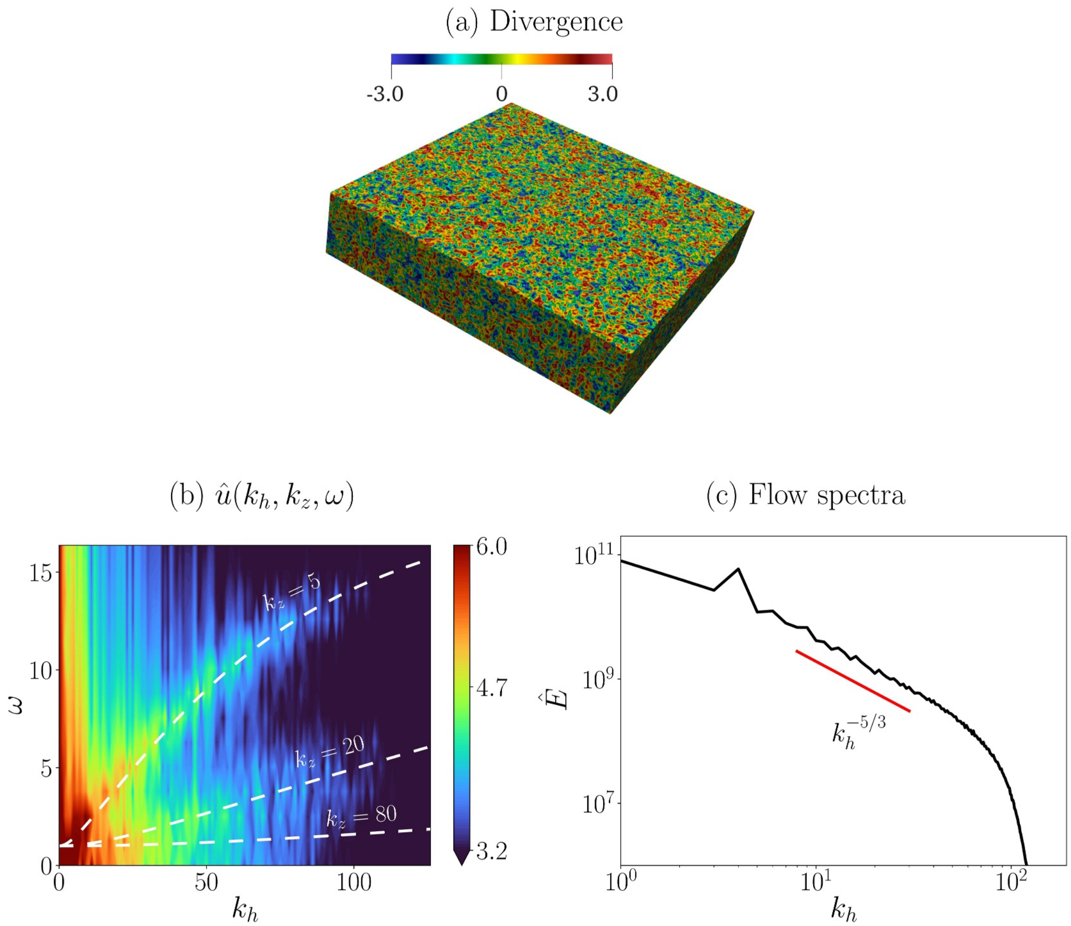

Figure 7. (a) Horizontal divergence of the flow. (b) x-component of the velocity field is plotted in the frequency-wavenumber space. White lines represent the dispersion relations corresponding to different vertical wavenumbers k_z. (c) Energy spectra for $\epsilon = 1$ case along with red line representing $k_h^{-5/3}$ power law for reference.

For $\epsilon = 0.1$, the tracer structures remain relatively at large scales and very low dissipation is seen in Figure 6h. In contrast, for $\epsilon = 0.3$, $\epsilon = 0.6$, and $\epsilon = 1.0$, the tracer fields become progressively stirred and mixed, leading to a monotonic increase in dissipation. This indicates enhanced mixing of the tracer field when we increase the value of ϵ. These observations align with our findings from previous experiments that had only discrete non-interacting waves, although the present wave field from RSW has nonlinear wave interactions and broadening of the frequency spectra beyond the dispersion curve.

4.2. Boussinesq Equations

We next consider the rotating nonhydrostatic Boussinesq equations, which contain three dimensional flow dynamics and vertical stratification. By evolving the forced-dissipative Boussinesq equations, we first obtained an equilibriated wave-dominant flow and benchmarked its features with previous studies. Appendix E contains details on the governing equations and our numerical setup for solving the equations. In Figure 7a we show the horizontal divergence $(\nabla \cdot \boldsymbol{v})$ obtained for the flow on the bottom half of the domain with top surface being the $z = 1.5\pi$ plane and bottom surface being the $z = 0$ plane. High divergence values and small scale signatures indicate the dominant presence of waves in the flow. Figure 7b shows the frequency-horizontal wavenumber spectrum of the flow for different values of vertical wavenumber, k_z. The white dashed lines in the figure denote dispersion lines and considerable overlapping of the bright region with the dispersion lines is observed. The dispersion relation associated with the linear internal waves is provided in Appendix E. In contrast to the kinematic models, here again, we see spread of the bright region around the dispersion lines due to nonlinear

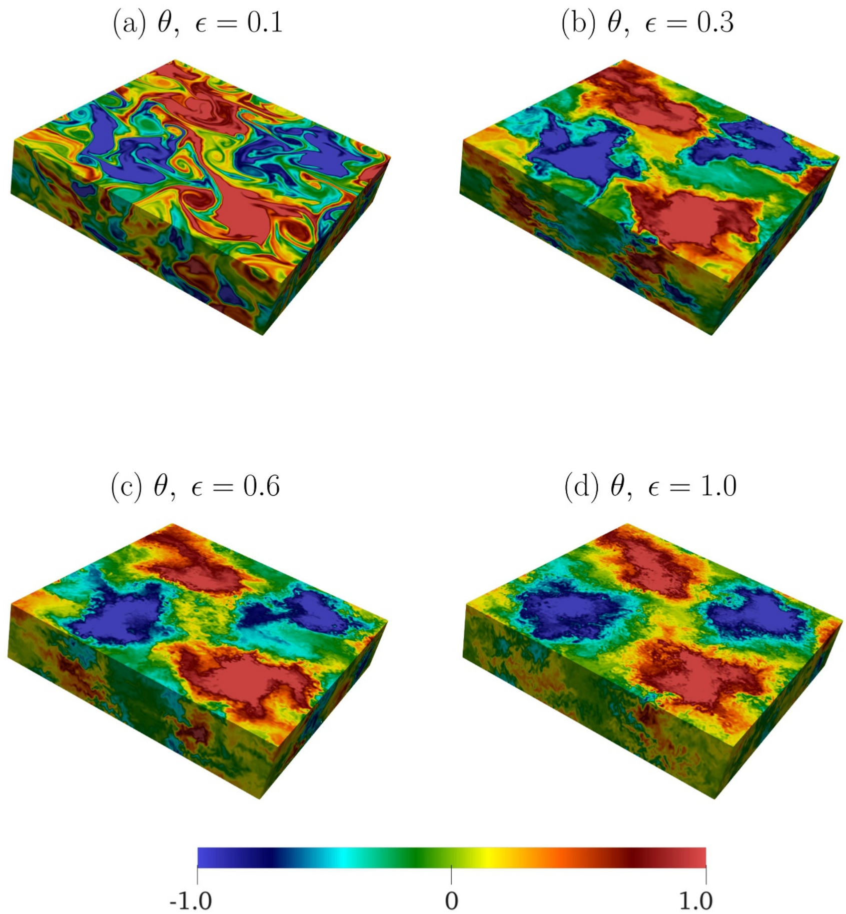

Figure 8. Tracer field structure for different values of ϵ are shown. Visually, one can note the increase in small scale features of the tracer with increase in ϵ.

interactions, as in RSW. Looking at the distribution of flow energy across different horizontal wavenumbers, k_h, in Figure 7c, we find that the spectrum almost follows a $-5/3$ power law.

Now that we have an equilibrated three-dimensional flow field $(\boldsymbol{v}, w)$ obtained by evolving the Boussinesq equations, we advect tracers according to the equation

$$\frac{\partial \theta}{\partial t} + \boldsymbol{v} \cdot \nabla \theta + w \frac{\partial \theta}{\partial z} = F - D \tag{21}$$

where F and D are the forcing and dissipation terms, respectively. Similar to the procedure followed in the RSW model, here as well, wave amplitude effects are investigated by scaling the flow fields from the Boussinesq equations by ϵ, such that $(\boldsymbol{v}, w) \rightarrow (\epsilon \boldsymbol{v}, \epsilon w)$, and then advecting the tracer field following Equation 21. Appendix E provides more details on the numerical setup, dissipation term, and forcing used for integrating Equation 21.

Figure 8 shows the steady state tracer field structures obtained for different values of ϵ, with the top and bottom surfaces being the same as in Figure 7a. Note that in all the cases, large scale structures are present because of the implemented large scale tracer forcing. While we observe more large scale structures in Figures 8a and 8b for the $\epsilon = 0.1$ and $\epsilon = 0.3$ cases, respectively, small scale structures are prominent in $\epsilon = 0.6$ and $\epsilon = 1$ cases (Figures 8c and 8d respectively). This observation provides a visual indication on the enhancement of tracer dispersion with increase in the value of ϵ.

We computed the time-averaged tracer variance spectra in all cases and these are shown in Figure 9a. The spectra are computed in the same manner as in the kinematic models, except that here the total wavenumber is defined as

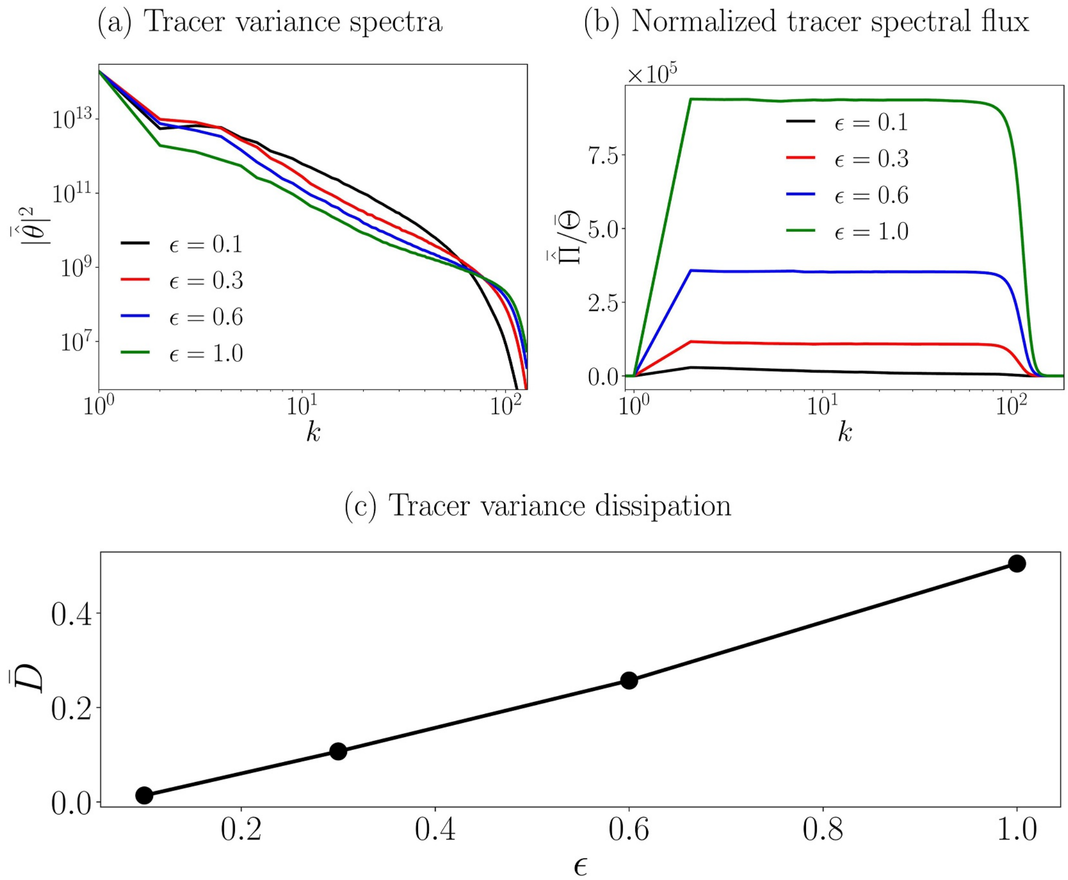

Figure 9. To quantify tracer stirring and mixing, time-averaged tracer variance spectra (a) and normalized time-averaged tracer spectral flux (b) are plotted. (c) Time-averaged tracer variance dissipation is plotted as a function of ϵ.

$k = \sqrt{k_h^2 + k_z^2}$. As expected from the forcing scheme, all cases exhibit the same tracer variance at $k = 1$. Beyond this forcing scale, however, clear differences emerge. For instance, when $\epsilon = 1$, the tracer variance spectrum drops sharply at low wavenumbers, and the tracer content is substantially reduced across almost the entire inertial range compared to smaller values of ϵ. This indicates more efficient stirring in the high wave amplitude case. As ϵ decreases, tracer variance progressively increases at intermediate wavenumbers, reflecting weaker stirring and reduced transfer of variance to small scales. The spectra also become noticeably shallower with decreasing ϵ. These trends closely mirror those observed in the earlier kinematic models with a spectrum of non-interacting waves. We also looked at the impact of wave amplitude on the horizontal $\left(|\hat{\bar{\theta}}|^2(k_h)\right)$ and vertical $\left(|\hat{\bar{\theta}}|^2(k_z)\right)$ tracer variance spectra and these showed similar results (figures omitted).

We computed time-averaged normalized tracer variance spectral flux as discussed in Section 3. Note from Figure 9b that the time-averaged tracer spectral flux values are positive in the inertial range and hence confirm downscale cascade of the tracer variance. With increasing ϵ, normalized tracer spectral flux values increase, suggesting that tracer cascade is more efficient with increasing values of ϵ. Time-averaged horizontal $\left(\hat{\bar{\Pi}}(k_h)\right)$ and vertical $\left(\hat{\bar{\Pi}}(k_z)\right)$ tracer fluxes also exhibited similar behavior. Furthermore, as seen from the RSW model, time-averaged tracer dissipation monotonically increases with increase in ϵ, this being shown in Figure 9c. Thus, despite the presence of nonlinear wave–wave interactions in the dynamic models, the overall influence of wave amplitude on tracer dispersion remains consistent with the behavior seen in the kinematic framework.

Our simulations with the dynamic models reveal that the presence of a spectrum of waves having $\mathcal{O}(1)$ amplitude can enhance the stirring and mixing of tracers. In a recent study, using the Boussinesq equations, Sanjay and

Thomas (2025) have showed that a flow dominated by $\mathcal{O}(1)$ amplitude waves is about 20 times more efficient in dispersing passive tracer field than an eddy-rich flow. Although the dynamic models include wave–wave interactions and associated second-order effects, which were absent in the kinematic setups discussed earlier, both approaches yield similar trends with respect to ϵ. A spectrum of finite amplitude or $\mathcal{O}(1)$ waves can therefore efficiently stir and mix tracers, this finding stemming from kinematic and dynamic models.

5. Summary and Discussion

The oceans contain fast fluctuating wave fields having frequencies ranging from inertial to the buoyancy frequency. These waves are responsible for the downscale cascade of flow kinetic energy and dissipation, thereby assisting in diapycnal mixing in the oceans. However, their impact on lateral dispersion of tracers is not appreciated, inspiring this study. We explored stirring and mixing of passive tracers by waves taking advantage of a series of kinematic and dynamic models.

We started by investigating how a single plane wave, propagating in an arbitrary direction, affects a passive tracer. Corresponding tracer advection equation was solved analytically and the solution revealed that the tracer field experiences only a reversible stretching such that it returns back to its initial state over a period of time. The solution further showed that small-amplitude waves induce only minor excursions of the tracer field before it returns to its initial state, whereas larger amplitude waves produce noticeably greater displacements. Yet, regardless of the wave amplitudes, the tracer field ultimately returns to its initial configuration. These observations indicated the inefficiency of a single plane wave, even with finite amplitude, in the stirring and mixing of a passive tracer field.

We continued our study by looking at tracer advection with a flow composed of two plane waves propagating in arbitrary directions. Analysis of the corresponding tracer advection equation helped us identify a family of curves, defined as $G(x, y, t) = C$, such that any arbitrarily initialized tracer field gets stretched in a direction perpendicular to G and gradually gets aligned with the isolines of G. This stretching and aligning process produced thin tracer filaments which can lead to dissipation and mixing at smaller scales. However, it was interesting to note that once the tracer field gets completely aligned with the isolines of G, no further stirring of the tracer field was observed. Numerical simulations supported these analytical findings and we quantified tracer mixing by looking at the decay of tracer variance over time. As found from the analysis, once the tracer field completely aligned with the contours, no further decay of tracer variance was observed. Examination of wave amplitude effects on tracer dispersion revealed that increasing wave amplitudes led to increased dissipation of tracer variance, highlighting the enhancement of tracer dispersion with wave amplitude. Small amplitude waves are far less effective in dispersing tracers than waves of order-one amplitude or finite amplitude waves. We also found that when two waves propagate in collinear directions, with equal magnitudes for the phase speed, the flow behaves like the single wave case and the tracer field returns to its initial state after a finite period without any net dispersion. Overall, our exploration of two plane waves' dynamics showed that two non-interacting and non-collinear waves are sufficient to stir and mix a passive tracer field, with dispersion increasing with wave amplitude.

To see if adding more waves enhanced tracer dispersion, we studied tracer dynamics in a flow composed of three plane waves. In this case, we numerically solved the tracer advection equation and found no sign regarding the existence of attractors similar to the G curves in the two-wave case. Instead, we observed continuous and sharp decay of tracer variance which indicated much more enhanced mixing of tracer variance in the three-wave case compared to the two-wave case. Further, we obtained steeper tracer variance spectrum compared to the two-wave case. Increasing wave amplitudes were also seen to increase tracer dispersion.

In realistic ocean conditions, the flow field is often composed of a broad spectrum of internal waves spanning a wide range of frequencies and propagating in different directions. This spectral nature of oceanic motions is well documented through observations and forms the basis of the Garrett–Munk spectrum (Garrett & Munk, 1972). Motivated by this, we extended our study to consider tracer advection in a flow constructed from a spectrum of non-interacting plane waves. For this, we set up three different flows having 1, 10, and 128 wave modes and evolved tracers to reach forced-dissipative equilibrium. As we moved from one mode case to the 128 modes' case, we observed steepening of tracer variance spectra and increasing tracer spectral flux, all indicative of enhancement in tracer stirring and mixing. These observations once again confirmed that increasing number of waves in the flow leads to efficient dispersion of tracer field. Further, in each case, we also checked the impact of varying wave amplitudes on the tracer dispersion by computing the normalized time-averaged tracer variance spectral flux. We obtained monotonic increase in the downscale cascade of tracer variance with increase in the wave amplitudes, indicating the role of wave amplitudes in increasing the efficiency of stirring the tracer field. In all of these experiments, the velocity fields were constructed from kinematic models and hence contain purely linear waves that do not interact with each other. These results therefore suggest that pure linear non-interacting waves having order-one amplitudes can efficiently stir and mix tracers.

We also performed tracer dispersion experiments with two dynamic models: RSW and Boussinesq equations. In both cases, we dynamically evolved the velocity fields from the corresponding nonlinear equations and tracers were advected by the flow field, after the flows achieved an equilibrated state. Examination of the obtained flow field in the frequency-wavenumber domain, in both models, showed significant spread around linear dispersion lines. This shows that, in contrast to the kinematic models that include only pure linear plane waves exactly obeying the dispersion relation, the dynamic models support not just linear wave behavior but also the second-order contributions produced by nonlinear interactions within the flow. In these cases as well, we evolved forced-dissipative tracer equations to obtain equilibrium condition for the tracer field and quantified tracer mixing by computing the tracer variance dissipation, spectra, and flux. We focused on the impact of wave amplitudes on tracer dispersion and found that finite amplitude wave fields significantly enhanced tracer dispersion. In both RSW and Boussinesq models, we observed that the tracer dissipation was monotonically increasing with increase in the wave amplitude values. This observation indicated that increasing wave amplitudes increased the downscale transfer of tracer variance and hence more tracer variance reached small scales, where it is dissipated. Our kinematic and dynamic model based results thus show that increasing the wave amplitudes can enhance tracer dispersion, despite the fundamental difference between non-interacting and interacting waves. Even though the dynamic models contain second order interaction effects, similarity with kinematic studies highlight that linear wave motions themselves play a dominant role in tracer dispersion. Thus, findings reported in this study evidently indicate that leading order wave effects have direct role in stirring and mixing of tracers.

Past oceanic studies have shown that submesoscale dynamics play a central role in setting vertical fluxes of mass, buoyancy, and tracers (Capet et al., 2008; L. N. Thomas et al., 2008). More recent work further demonstrates that adequately resolving submesoscale motions is essential for capturing the eastward extension of Gulf Stream into the interior of North Atlantic and the downward transfer of eddy kinetic energy (Chassignet & Xu, 2017). Modern ocean models therefore strive to represent submesoscale processes because of their well-established importance. As noted in the introduction, internal waves with order-one amplitudes are energetically active at these same submesoscales. However, they remain only partially resolved or in many cases, entirely unresolved, in current modeling frameworks. Our results show that leading order linear waves having finite amplitudes can generate substantial lateral transport and mixing of tracers, contradicting the long-held assumption that waves simply oscillate tracers about their mean position without producing net dispersion. This implies that internal waves may contribute directly to the effective isopycnal diffusivity and, to some extent, may explain the observed enhanced stirring of tracers at submesoscales (Klymak et al., 2015; Kunze et al., 2015; Shcherbina et al., 2015; Spiro Jaeger et al., 2020). Recent studies also emphasize the need for high-resolution regional simulations to better capture the internal wave spectrum and its dynamical impacts (Nelson et al., 2020; Savage, Arbic, Alford, et al., 2017; Savage, Arbic, Richman, et al., 2017). Together with these findings, our results reinforce the growing consensus that internal-wave-driven dispersion must be either explicitly resolved or carefully parameterized in global ocean models. Improving the representation of wave-induced mixing will be crucial for reducing tracer biases, refining estimates of isopycnal mixing, and ultimately improving predictions of climate variability.

Appendix A: Analytical Solution for Tracer Dispersion by a Single Plane Wave

For the single wave case, let us consider the tracer evolution Equation 6

$$\frac{\partial \theta}{\partial t} + 2\epsilon k_y \sin(\boldsymbol{k}\cdot\boldsymbol{x} - \omega t + \phi)\frac{\partial \theta}{\partial x} - 2\epsilon k_x \sin(\boldsymbol{k}\cdot\boldsymbol{x} - \omega t + \phi)\frac{\partial \theta}{\partial y} = 0. \tag{A1}$$

This equation can be solved by using the method of characteristics (MOC) where the characteristic equations are:

$$\frac{\mathrm{d}\theta}{\mathrm{d}t} = 0 \tag{A2a}$$

$$\frac{\mathrm{d}x}{\mathrm{d}t} = 2\epsilon k_y \sin(\boldsymbol{k}\cdot\boldsymbol{x} - \omega t + \phi) \tag{A2b}$$

$$\frac{\mathrm{d}y}{\mathrm{d}t} = -2\epsilon k_x \sin(\boldsymbol{k}\cdot\boldsymbol{x} - \omega t + \phi). \tag{A2c}$$

Equation A2a indicates that along the characteristics defined by (x, y), the tracer field remains constant, such that $\theta(\boldsymbol{x}, t) = \theta_0(\boldsymbol{x_0}, 0)$, with $\boldsymbol{x_0} = (x_0, y_0)$ being the initial position vector. To proceed further, we substitute

$$\chi = \boldsymbol{k}\cdot\boldsymbol{x} - \omega t = k_x x + k_y y - \omega t$$

which leads to

$$\frac{\mathrm{d}\chi}{\mathrm{d}t} = k_x\frac{\mathrm{d}x}{\mathrm{d}t} + k_y\frac{\mathrm{d}y}{\mathrm{d}t} - \omega \tag{A3}$$

Using Equations A2b and A2c in Equation A3, we get

$$\frac{\mathrm{d}\chi}{\mathrm{d}t} = -\omega \quad \text{or} \quad \chi = \chi_0 - \omega t \tag{A4}$$

where $\chi_0 = k_x x_0 + k_y y_0$. Above equation suggests that along the characteristics, χ_0 is a constant, implying that

$$\chi_0 = k_x x_0 + k_y y_0 = \boldsymbol{k}\cdot\boldsymbol{x}. \tag{A5}$$

Now, substituting Equation A4 in Equations A2b and A2c, we get

$$\frac{\mathrm{d}x}{\mathrm{d}t} = 2\epsilon k_y \sin(\chi_0 - \omega t + \phi) \tag{A6}$$

$$\frac{\mathrm{d}y}{\mathrm{d}t} = -2\epsilon k_x \sin(\chi_0 - \omega t + \phi) \tag{A7}$$

Integrating above equations from 0 to t, we get:

$$x = x_0 + \frac{2\epsilon k_y}{\omega}\left[\cos(\chi_0 - \omega t + \phi) - \cos(\chi_0 + \phi)\right] \tag{A8}$$

$$y = y_0 - \frac{2\epsilon k_x}{\omega}\left[\cos(\chi_0 - \omega t + \phi) - \cos(\chi_0 + \phi)\right] \tag{A9}$$

Substituting for χ_0 using Equation A5 in the above equations and rearranging, we get:

$$x_0 = x - \frac{2\epsilon k_y}{\omega}\left[\cos(\boldsymbol{k}\cdot\boldsymbol{x} - \omega t + \phi) - \cos(\boldsymbol{k}\cdot\boldsymbol{x} + \phi)\right] \tag{A10}$$

$$y_0 = y + \frac{2\epsilon k_x}{\omega}\left[\cos(\boldsymbol{k}\cdot\boldsymbol{x} - \omega t + \phi) - \cos(\boldsymbol{k}\cdot\boldsymbol{x} + \phi)\right] \tag{A11}$$

Now, as mentioned above, from Equation A2a, we note that along the trajectories, θ is a constant, implying that:

$$
\begin{aligned}
\theta(\boldsymbol{x},t) &= \theta_0(\boldsymbol{x}_0,0)\\
&= \theta_0\Bigg(x-\frac{2\epsilon k_y}{\omega}[\cos(\boldsymbol{k}\cdot\boldsymbol{x}-\omega t+\phi)-\cos(\boldsymbol{k}\cdot\boldsymbol{x}+\phi)],\\
&\qquad y+\frac{2\epsilon k_x}{\omega}[\cos(\boldsymbol{k}\cdot\boldsymbol{x}-\omega t+\phi)-\cos(\boldsymbol{k}\cdot\boldsymbol{x}+\phi)]\Bigg).
\end{aligned}
\tag{A12}
$$

Thus, Equation A12 forms the exact solution for the tracer field advected by a single wave field having the wave vector $\boldsymbol{k}$ and frequency ω.

Appendix B: Tracer Stretching by Two Plane Waves

The governing equation for a tracer field advected by two arbitrary waves can be written in the transformed coordinates as

$$\frac{\partial\theta}{\partial T}+(2\epsilon_2 K\sin Y-\omega_1)\frac{\partial\theta}{\partial X}+(-2\epsilon_1 K\sin X-\omega_2)\frac{\partial\theta}{\partial Y}=0. \tag{B1}$$

Now, we can apply MOC to the above equation such that the characteristic equations will be

$$\frac{\mathrm{d}\theta}{\mathrm{d}T}=0 \tag{B2a}$$

$$\frac{\mathrm{d}X}{\mathrm{d}T}=2\epsilon_2 K\sin Y-\omega_1 \tag{B2b}$$

$$\frac{\mathrm{d}Y}{\mathrm{d}T}=-2\epsilon_1 K\sin X-\omega_2 \tag{B2c}$$

As in the case of single wave, here as well we conclude from Equation B2a that the tracer field is constant along the trajectories defined by (X,Y). Dividing Equation B2b by Equation B2c, we get:

$$\frac{dX}{dY}=\frac{2\epsilon_2 K\sin Y-\omega_1}{-2\epsilon_1 K\sin X-\omega_2}. \tag{B3}$$

Integrating the above equation gives us

$$G(X,Y)=2K(\epsilon_1\cos X+\epsilon_2\cos Y)+\omega_1 Y-\omega_2 X=C. \tag{B4}$$

G from the above equation can be used to rewrite Equation B1 as

$$\frac{\partial\theta}{\partial T}+\left(\widetilde{\nabla}^{\perp}G\right)\cdot\widetilde{\nabla}\theta=0 \tag{B5}$$

As mentioned in the main section, Equation B5 shows that the tracer gets stretched only in the direction perpendicular to the level sets defined by G. Additionally, it can be easily noted that any function of G will be an exact solution of Equation B5, as discussed in the main section.

B1. Two Plane Waves Propagating in Opposite Directions With Same Magnitude for Wavenumber Vectors

Let us consider an example where one wave is propagating in the positive x direction and another one in the negative x direction. The corresponding streamfunction will be

$$\psi(x,y,t)=2\epsilon_1\cos(x-\omega_1 t+\phi_1)+2\epsilon_2\cos(x+\omega_2 t+\phi_2). \tag{B6}$$

Using the above form to compute the velocity fields and substituting it in Equation 1, we obtain

$$\frac{\partial\theta}{\partial t} + \left(-2\epsilon_1 \sin\left(x - \omega_1 t + \phi_1\right) - 2\epsilon_2 \sin\left(x + \omega_2 t + \phi_2\right)\right)\frac{\partial\theta}{\partial y}. \tag{B7}$$

Now, we can apply MOC on above equation by identifying the characteristics equations as

$$\frac{\mathrm{d}\theta}{\mathrm{d}t} = 0 \tag{B8a}$$

$$\frac{\mathrm{d}x}{\mathrm{d}t} = 0 \tag{B8b}$$

$$\frac{\mathrm{d}y}{\mathrm{d}t} = -2\epsilon_1 \sin\left(x - \omega_1 t + \phi_1\right) - 2\epsilon_2 \sin\left(x + \omega_2 t + \phi_2\right) \tag{B8c}$$

While Equation B8a suggests that the tracer field is constant along the trajectories defined by x and y, from Equation B8b we note that $x = x_0$, x_0 being the initial location. Using this, we can solve Equation B8c to obtain

$$y_0 = y + \frac{2\epsilon_1}{\omega_1}\left[\cos\left(x - \omega_1 t + \phi_1\right) - \cos\left(x + \phi_1\right) - \frac{2\epsilon_2}{\omega_2}\left[\cos\left(x + \omega_2 t + \phi_2\right) - \cos\left(x + \phi_2\right)\right]\right. \tag{B9}$$

Using x_0 and y_0, we can obtain the exact solution $\theta(\boldsymbol{x}, t)$, given the general initial condition $\theta_0(\boldsymbol{x_0}, 0)$, as

$$\theta(\boldsymbol{x}, t) = \theta_0\left(x, y + \frac{2\epsilon_1}{\omega_1}\left[\cos\left(x - \omega_1 t + \phi_1\right) - \cos\left(x + \phi_1\right)\right] - \frac{2\epsilon_2}{\omega_2}\left[\cos\left(x + \omega_2 t + \phi_2\right) - \cos\left(x + \phi_2\right)\right]\right) \tag{B10}$$

In the above example, magnitudes of the wavenumber vectors were the same and hence we have $\omega_1 = \omega_2$. Note from Equation B10 that the tracer field can return to its initial state over a period $\tau = 2\pi/\omega_1 = 2\pi/\omega_2$. Thus, this is a typical example of the two wave configuration where we do not see any stretching or mixing of the tracer field. However, even when the waves are propagating in collinear direction, if their magnitudes of the wavenumber vectors differ, the tracer field cannot reach exactly back to its initial state. This can eventually lead to the mixing of tracer field over a long interval of time.

Appendix C: Tracer Spectra for Different Configurations of Three Waves

Figure C1 shows the evolution of tracer variance spectra for different three wave configurations with varying amplitudes. As in Figure 3d, tracer variance spectra evolve much more slowly for small-amplitude waves, where $\epsilon_1 = \epsilon_2 = \epsilon_3 = 0.1$ (dashed curves) than for finite-amplitude waves, where $\epsilon_1 = \epsilon_2 = \epsilon_3 = 1$ (solid curves). The low-amplitude cases exhibit nearly identical spectral evolution and comparable levels of tracer variance decay across all three configurations. In contrast, while the qualitative behavior of the finite-amplitude cases are similar, there are differences in the magnitude of tracer variance decay across the three cases.

10.1029/2026AV002429

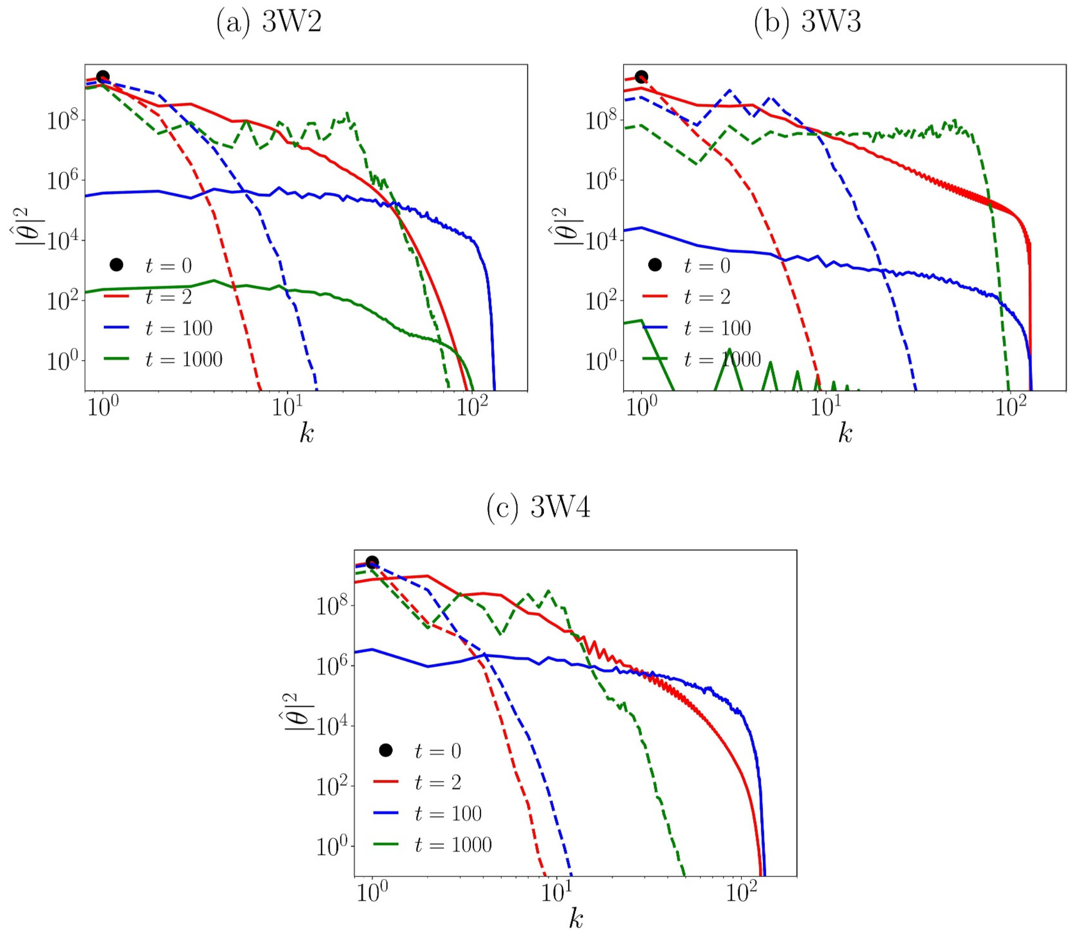

Figure C1. Tracer variance spectra evolution in the three wave configurations 3W2 (a), 3W3 (b), and 3W4 (c) are shown. The solid lines in each case correspond to $\epsilon_1 = \epsilon_2 = \epsilon_3 = 1$ and dashed lines correspond to $\epsilon_1 = \epsilon_2 = \epsilon_3 = 0.1$. Note that the green solid lines, corresponding to $t = 1000$, is only partly visible in 3W3 and absent in 3W4, indicating that decay strength is more in 3W4, followed by 3W3, and then 3W2.

Appendix D: Spectral Binning

To obtain a one dimensional spectrum from a two-dimensional spectral field defined on the wavenumber space (k_x, k_y), we first convert each mode to its isotropic wavenumber $k = \sqrt{k_x^2 + k_y^2}$. The spectrum is then constructed by grouping all modes according to their wavenumber magnitude. We define a set of non-overlapping wavenumber bins, and all spectral values whose wavenumber magnitude falls within a particular bin are summed together and associated with a representative wavenumber for that bin. For example, modes with $0 \leq k < 0.5$ are assigned to $k = 0.5$, modes with $0.5 \leq k < 1.5$ are assigned to $k = 1$, those with $1.5 \leq k < 2.5$ to $k = 2$, and so on. Each bin therefore collects contributions from an annular region in the two dimensional spectral domain, yielding a discrete one dimensional spectrum as a function of wavenumber. This binning procedure is general and can be applied to three dimensions as well, where $k = \sqrt{k_x^2 + k_y^2 + k_z^2}$.

Appendix E: Numerical Methods

E1. Kinematic Model Simulations

In all the kinematic model experiments discussed in the manuscript, Equation 1 was numerically integrated using a pseudospectral method over a two-dimensional periodic square domain of size $2\pi \times 2\pi$, resolved with 384^2 uniformly spaced grid points. Time stepping was carried out with a fourth-order Runge–Kutta (RK4) scheme.

Only for the Gaussian initialization in two-wave case, we used a periodic square domain of size $6\pi \times 6\pi$ with 1152^2 uniformly spaced grid points so that the tracer stretching can be visualized more clearly.

For the two-wave and three-wave cases, a small-scale dissipation term of the form $D = \nu_\theta \Delta^8 \theta$ was added along with Equation 1, where $\nu_\theta = 10^{-32}$ is the hyperviscosity and $\Delta = \partial^2/\partial x^2 + \partial^2/\partial y^2$ denotes the two dimensional Laplacian operator. This choice of an eighth-order hyperdiffusion ensures that dissipation acts predominantly at the smallest resolved scales, allowing a wide range of inviscid scales to be sustained in the flow. For the Gaussian blob case, because of the domain size difference, we used $\nu_\theta = 10^{-42}$.

For kinematic experiments involving more than three waves, in addition to the dissipation term described above, a forcing term was introduced as in Equation 18 to achieve a statistically steady state for the tracer field. This forcing was implemented in spectral space by maintaining the initial tracer variance at small wavenumbers throughout the simulation. Specifically, we maintained the tracer variance at wavenumber $k = \sqrt{2}$.

E2. Rotating Shallow Water Simulations

The rotating shallow water (RSW) model in nondimensional form is given by

$$\frac{\partial \boldsymbol{v}}{\partial t} + \boldsymbol{f} \times \boldsymbol{v} + \nabla h + \beta \boldsymbol{v} \cdot \nabla \boldsymbol{v} = \boldsymbol{F}_v - \boldsymbol{D}_v \tag{E1a}$$

$$\frac{\partial h}{\partial t} + \nabla \cdot \boldsymbol{v} + \beta(\nabla \cdot (h\boldsymbol{v})) = F_h - D_h. \tag{E1b}$$

Above, $\boldsymbol{v}$ is the velocity field and h is the height field. $\boldsymbol{f} = f\hat{z}$ with f being the inertial frequency and $\hat{z}$ is the unit vector in the z direction. We set $f = 1$ in our simulations. The nondimensional parameter β, the Froude number, is defined as the ratio of flow velocity scale to the phase speed of non-rotating gravity waves. We chose $\beta = 0.1$, a small value, placing the system in a weakly nonlinear regime. In such a limit, we can perform a decomposition of the velocity field into balanced mode, which satisfy geostrophic balance condition, and wave modes which are an exact solution of the linear part of Equations E1a and E1b. This decomposition is used in several previous works (Majda & Embid, 1998; Remmel & Smith, 2009; J. Thomas & Yamada, 2019; Ward & Dewar, 2010; Warn, 1986). The terms $\boldsymbol{F}_v$ and F_h denote the forcing on the velocity and height fields respectively. These forcings are the same as those used in J. Thomas et al. (2024) and we refer to Appendix A therein for more details. The hyperdissipation terms for the velocity and height fields are denoted as $\boldsymbol{D}_v = \nu\Delta^2\boldsymbol{v}$ and $D_h = \nu\Delta^2 h$ with $\nu = 8.45 \times 10^{-8}$ such that the terms restrict dissipation to the smallest resolved scales in flow. More details on obtaining the nondimensionalized equations, decomposition of flow, and implementation of the forcing can be found in J. Thomas et al. (2024).

In the dynamic RSW model, both the flow and tracer equations were evolved simultaneously using a pseudo-spectral method in a periodic domain of length 2π in each direction, discretized on a 768^2 grid. Time stepping for both the flow and tracer was carried out using the RK4 scheme. The tracer equation, Equation 18, was evolved using the velocity field from RSW equations at each time step, where the dissipation term for the tracer equation was $D = \nu_\theta \Delta^2 \theta$ with $\nu_\theta = 8.45 \times 10^{-8}$. The forcing was same as in the kinematic model experiment with more than three waves. To eliminate aliasing errors arising from nonlinear terms, the standard 2/3 dealiasing rule was applied, which retains only the lowest $N/3$ positive and negative wavenumbers in each direction, where N is the total number of grid points in each direction.

E3. Boussinesq Model Simulations

The Boussinesq equations in nondimensional form are

$$\frac{\partial \boldsymbol{v}}{\partial t} + \hat{z} \times \boldsymbol{v} + \nabla p + Ro\left(\boldsymbol{v} \cdot \nabla \boldsymbol{v} + w\frac{\partial \mathbf{v}}{\partial z}\right) = \boldsymbol{F}_v - \boldsymbol{D}_v \tag{E2a}$$

$$\frac{\partial w}{\partial t} + \alpha^2\left(\frac{\partial p}{\partial z} - b\right) + Ro\left(\boldsymbol{v} \cdot \nabla w + w\frac{\partial w}{\partial z}\right) = F_w - D_w \tag{E2b}$$

$$\frac{\partial b}{\partial t} + w + Ro\left(\boldsymbol{v}\cdot\nabla b + w\frac{\partial b}{\partial z}\right) = F_b - D_b \tag{E2c}$$

$$\nabla\cdot\boldsymbol{v} + \frac{\partial w}{\partial z} = 0 \tag{E2d}$$

where $\boldsymbol{v} = (u, v)$ is the horizontal velocity vector, w is the vertical velocity, p is the pressure, b is the buoyancy, and $\hat{z}$ is the unit vector along the vertical direction. The parameter Ro is the Rossby number, which is the ratio of inertial force to the Coriolis force and α is the ratio of buoyancy frequency to the inertial frequency. In this study we restrict ourselves to low Rossby limit by using $Ro = 0.1$ and set $\alpha = 20$. The variables $\boldsymbol{F_v}$, F_w, and F_b in Equations E2a–E2d denote forcing on the flow fields $\boldsymbol{v}$, w, and b respectively. The dissipation terms are $\boldsymbol{D_v}$, D_w, and D_b which are represented as $\nu\Delta_{3D}^8\boldsymbol{v}$, $\nu\Delta_{3D}^8 w$, and $\nu\Delta_{3D}^8 b$, respectively, where $\nu = 10^{-32}$ and $\Delta_{3D} = \partial^2/\partial x^2 + \partial^2/\partial y^2 + \partial^2/\partial z^2$ is the three dimensional Laplacian operator.

As in the RSW model, here also we can decompose the velocity field into a balanced part which satisfies the geostrophic and hydrostatic balances, and a wave part which obeys the linear part of Equations E2a–E2d in the absence of forcing and dissipation (Bartello, 1995; Herbert et al., 2016; Hernandez-Duenas et al., 2021; Smith & Waleffe, 2002; J. Thomas & Daniel, 2020). The linear wave part follows a dispersion relation, in nondimensional form, given by $\omega^2 = \alpha^2\left(k_h^2 + k_z^2\right)/\left(k_h^2 + \alpha^2 k_z^2\right)$ where $k_h = \sqrt{k_x^2 + k_y^2}$ is the horizontal wavenumber and k_z is the vertical wavenumber. We have used the same numerical setup, which include the forcing and dissipation terms, as in Sanjay and Thomas (2025) to obtain a steady state wave-dominated flow. See Appendix A of Sanjay and Thomas (2025) for more details on the forcing scheme.

For the Boussinesq model, the full set of equations and the tracer advection Equation 21 were integrated simultaneously in a three-dimensional periodic domain of size $(2\pi)^3$, discretized with 384^3 grid points. The dissipation term for the tracer equation was $D = \nu_\theta\Delta^8\theta$, with $\nu_\theta = 10^{-32}$ and as in the kinematic and RSW simulations, the tracer was forced to maintain constant variance at $k = \sqrt{k_h^2 + k_z^2} = \sqrt{2}$, thereby sustaining a statistically steady state. Time integration for both the flow and tracer equations was performed using the RK4 method and 2/3 dealiasing rule was implemented to prevent aliasing errors.

Conflict of Interest

The authors declare no conflicts of interest relevant to this study.

Availability Statement

The data used for this manuscript are available on Zenodo (Sanjay & Thomas, 2026).

Acknowledgments
JT is grateful to the Deep Ocean Mission scheme of the Ministry of Earth Sciences for providing financial support for this work through the project F.No. MoES/PAMC/DOM/18/2022 (E-12926). Both the authors acknowledge discussions that benefited this work from two meetings organized at the International Centre for Theoretical Sciences (ICTS): Mathematical modeling of Climate, Ocean, and Atmosphere processes (ICTS/COAPS2023/06) and Theoretical and Practical Perspectives in Geophysical Fluid Dynamics (ICTS/TAPGFD2024/ 05).

References

Abernathey, R., Gnanadesikan, A., Pradal, M., & Sundermeyer, M. A. (2022). Isopycnal mixing. In *Ocean mixing* (pp. 215–256). Elsevier.

Abernathey, R. P., & Marshall, J. (2013). Global surface eddy diffusivities derived from satellite altimetry. *JGR. Oceans*, *118*(2), 901–916. https://doi.org/10.1002/jgrc.20066

Alford, M., MacKinnon, J., Simmons, H., & Nash, J. (2016). Near-inertial internal gravity waves in the ocean. *Annual Review of Marine Science*, *8*(1), 95–123. https://doi.org/10.1146/annurev-marine-010814-015746

Alford, M. H. (2003). Energy available for ocean mixing redistributed through long-range propagation of internal waves. *Nature*, *423*, 159–163.

Arbic, B. K. (2022). Incorporating tides and internal gravity waves within global ocean general circulation models: A review. *Progress in Oceanography*, *206*, 102824. https://doi.org/10.1016/j.pocean.2022.102824

Balwada, D., Gray, A. R., Dove, L. A., & Thompson, A. F. (2024). Tracer stirring and variability in the Antarctic Circumpolar Current near the Southwest Indian ridge. *Journal of Geophysical Research: Oceans*, *129*(1), e2023JC019811. https://doi.org/10.1029/2023jc019811

Bartello, P. (1995). Geostrophic adjustment and inverse cascades in rotating stratified turbulence. *Journal of the Atmospheric Sciences*, *52*(24), 4410–4428. https://doi.org/10.1175/1520-0469(1995)052<4410:gaaici>2.0.co;2

Booth, J., & Kamenkovich, I. (2008). Isolating the role of mesoscale eddies in mixing of a passive tracer in an eddy resolving model. *Journal of Geophysical Research: Oceans*, *113*(C5), C05021. https://doi.org/10.1029/2007jc004510

Bühler, O., Grisouard, N., & Holmes-Cerfon, M. (2013). Strong particle dispersion by weakly dissipative random internal waves. *Journal of Fluid Mechanics*, *719*, R4. https://doi.org/10.1017/jfm.2013.71

Buhler, O., & Holmes-Cerfon, M. (2009). Particle dispersion by random waves in rotating shallow water. *Journal of Fluid Mechanics*, *638*, 5–26. https://doi.org/10.1017/s0022112009991091

Capet, X., McWilliams, J. C., Molemaker, M. J., & Shchepetkin, A. F. (2008). Mesoscale to submesoscale transition in the California current system. Part I: Flow structure, eddy flux, and observational tests. *Journal of Physical Oceanography*, *38*(1), 29–43. https://doi.org/10.1175/2007jpo3671.1

Chassignet, E. P., & Xu, X. (2017). Impact of horizontal resolution (1/12 to 1/50) on Gulf stream separation, penetration, and variability. *Journal of Physical Oceanography*, *47*(8), 1999–2021. https://doi.org/10.1175/jpo-d-17-0031.1

Cole, S., & Rudnick, D. (2012). The spatial distribution and annual cycle of upper ocean thermohaline structure. *Journal of Geophysical Research*, *117*(C2), C02027. https://doi.org/10.1029/2011jc007033

Cole, S., Rudnick, D., & Colosi, J. (2010). Seasonal evolution of upper-ocean horizontal structure and the remnant mixed layer. *Journal of Geophysical Research*, *115*(C4), C04012. https://doi.org/10.1029/2009jc005654

Ferrari, R., & Rudnick, D. (2000). Thermohaline variability in the upper ocean. *Journal of Geophysical Research*, *105*(C7), 16857–16884. https://doi.org/10.1029/2000jc900057

Garrett, C., & Munk, W. (1979). Internal waves in the ocean. *Annual Review of Fluid Mechanics*, *11*(3), 339–369.

Garrett, C., & Munk, W. (1972). Space-timescales of internal waves. *Geophysical Fluid Dynamics*, *2*(3), 225–264. https://doi.org/10.1080/03091927208236082

Gent, P. R., & McWilliams, J. C. (1990). Isopycnal mixing in ocean circulation models. *Journal of Physical Oceanography*, *20*(1), 150–155. https://doi.org/10.1175/1520-0485(1990)020<0150:imiocm>2.0.co;2

Gnanadesikan, A., Bianchi, D., & Pradal, M. (2013). Critical role for mesoscale eddy diffusion in supplying oxygen to hypoxic ocean waters. *Geophysical Research Letters*, *40*(19), 5194–5198. https://doi.org/10.1002/grl.50998

Gnanadesikan, A., Pradal, M. A., & Abernathey, R. (2015). Isopycnal mixing by mesoscale eddies significantly impacts oceanic anthropogenic carbon uptake. *Geophysical Research Letters*, *42*(11), 4249–4255. https://doi.org/10.1002/2015gl064100

Gregg, M. C., Sanford, T. B., & Winkel, D. P. (2003). Reduced mixing from the breaking of internal waves in equatorial waters. *Nature*, *422*(6931), 513–515. https://doi.org/10.1038/nature01507

Herbert, C., Marino, R., Rosenberg, D., & Pouquet, A. (2016). Waves and vortices in the inverse cascade regime of stratified turbulence with or without rotation. *Journal of Fluid Mechanics*, *806*, 165–204. https://doi.org/10.1017/jfm.2016.581

Hernandez-Duenas, G., Lelong, M.-P., & Smith, L. M. (2021). Impact of wave-vortical interactions on oceanic submesoscale lateral dispersion. *Journal of Physical Oceanography*, *51*(11), 3495–3511. https://doi.org/10.1175/jpo-d-20-0299.1

Holmes, R., Groeskamp, S., Stewart, K., & McDougall, T. (2022). Sensitivity of a coarse-resolution global ocean model to a spatially variable neutral diffusivity. *Journal of Advances in Modeling Earth Systems*, *14*(3), e2021MS002914. https://doi.org/10.1029/2021ms002914

Holmes-Cerfon, M., Buhler, O., & Ferrari, R. (2011). Particle dispersion by random waves in the rotating Boussinesq system. *Journal of Fluid Mechanics*, *670*, 150–175. https://doi.org/10.1017/s0022112010005240

Jones, C., & Abernathey, R. P. (2019). Isopycnal mixing controls deep ocean ventilation. *Geophysical Research Letters*, *46*(22), 13144–13151. https://doi.org/10.1029/2019gl085208

Jones, N., Ivey, G., Rayson, M., & Kelly, S. (2020). Mixing driven by breaking nonlinear internal waves. *Geophysical Research Letters*, *47*(19), e2020GL089591. https://doi.org/10.1029/2020gl089591

Katsumata, K., Talley, L., Capuano, T., & Whalen, C. (2021). Spatial and temporal variability of diapycnal mixing in the Indian Ocean. *JGR: Oceans*, *126*(7), e2021JC017257. https://doi.org/10.1029/2021jc017257

Klymak, J. M., Crawford, W., Alford, M. H., MacKinnon, J. A., & Pinkel, R. (2015). Along-isopycnal variability of spice in the North Pacific. *Journal of Geophysical Research: Oceans*, *120*(3), 2287–2307. https://doi.org/10.1002/2013jc009421

Kunze, E. (2017). Internal-wave-driven mixing: Global geography and budgets. *Journal of Physical Oceanography*, *47*(6), 1325–1345. https://doi.org/10.1175/jpo-d-16-0141.1

Kunze, E., Klymak, J. M., Lien, R. C., Ferrari, R., Lee, M. A., Sundermeyer, C. M., & Goodman, L. (2015). Submesoscale water-mass spectra in the Sargasso Sea. *Journal of Physical Oceanography*, *45*(5), 1325–1338. https://doi.org/10.1175/jpo-d-14-0108.1

Ledwell, J., Watson, A., & Law, C. (1993). Evidence for slow mixing across the pycnocline from an open-ocean tracer-release experiments. *Nature*, *364*(6439), 701–703. https://doi.org/10.1038/364701a0

Ledwell, J. R., St. Laurent, L. C., Girton, J. B., & Toole, J. M. (2011). Diapycnal mixing in the Antarctic circumpolar current. *Journal of Physical Oceanography*, *41*(1), 241–246.

Ledwell, J. R., Watson, A. J., & Law, C. S. (1998). Mixing of a tracer in the pycnocline. *Journal of Geophysical Research: Oceans*, *103*(C10), 21499–21529. https://doi.org/10.1029/98jc01738

Lien, R.-C., & Sanford, T. B. (2019). Small-scale potential vorticity in the upper ocean thermocline. *Journal of Physical Oceanography*, *49*(7), 1845–1872. https://doi.org/10.1175/jpo-d-18-0052.1

Majda, A., & Embid, P. (1998). Averaging over fast gravity waves for geophysical flows with unbalanced initial data. *Theoretical and Computational Fluid Dynamics*, *11*(3–4), 155–169. https://doi.org/10.1007/s001620050086

McWilliams, J. C. (2008). The nature and consequences of oceanic eddies. *Geophysical Monograph Series*, *177*, 5–15.

Müller, P., & Briscoe, M. (2000). Diapycnal mixing and internal waves. *Oceanography*, *13*(2), 98–103. https://doi.org/10.5670/oceanog.2000.40

Naveira Garabato, A. C., Oliver, K., Watson, A. J., & Messias, M. (2004). Turbulent diapycnal mixing in the Nordic seas. *Journal of Geophysical Research: Oceans*, *109*(C12). https://doi.org/10.1029/2004jc002411

Nelson, A., Arbic, B. K., Menemenlis, D., Peltier, W. R., Alford, M. H., Grisouard, N., & Klymak, J. M. (2020). Improved internal wave spectral continuum in a regional ocean model. *Journal of Geophysical Research: Oceans*, *125*(5), e2019JC015974. https://doi.org/10.1029/2019jc015974

Pinkel, R. (2014). Vortical and internal wave shear and strain. *Journal of Physical Oceanography*, *44*(8), 2070–2092. https://doi.org/10.1175/jpo-d-13-090.1

Polzin, K. L., & Ferrari, R. (2004). Isopycnal dispersion in NATRE. *Journal of Physical Oceanography*, *34*(1), 247–257. https://doi.org/10.1175/1520-0485(2004)034<0247:idin>2.0.co;2

Polzin, K. L., & Lvov, Y. (2011). Toward regional characterizations of the oceanic internal wavefield. *Reviews of Geophysics*, *49*(4), RG4003. https://doi.org/10.1029/2010rg000329

Qiu, B., Chen, S., Klein, P., Wang, J., Torres, H., Fu, L., & Menemenlis, D. (2018). Seasonality in transition scale from balanced to unbalanced motions in the world ocean. *Journal of Physical Oceanography*, *48*(3), 591–605. https://doi.org/10.1175/jpo-d-17-0169.1

Redi, M. H. (1982). Oceanic isopycnal mixing by coordinate rotation. *Journal of Physical Oceanography*, *12*(10), 1154–1158. https://doi.org/10.1175/1520-0485(1982)012<1154:oimbcr>2.0.co;2

Remmel, M., & Smith, L. (2009). New intermediate models for rotating shallow water and an investigation of the preference for anticyclones. *Journal of Fluid Mechanics*, *635*, 321–359. https://doi.org/10.1017/s0022112009007897

Salmon, R. (1978). *Lectures on geophysical fluid dynamics*. Oxford University Press.

Sanderson, B. G., & Okubo, A. (1988). Diffusion by internal waves. *Journal of Geophysical Research*, *93*(C4), 3570–3582. https://doi.org/10.1029/jc093ic04p03570

Sanjay, C. P., & Thomas, J. (2025). Enhanced passive tracer dispersion by an energetic internal wave continuum. *Journal of Geophysical Research: Oceans*, *130*(5), e2024JC021754. https://doi.org/10.1029/2024jc021754

Sanjay, C. P., & Thomas, J. (2026). Data and codes: Irreversible stirring and mixing of tracers by oceanic internal gravity waves [Dataset and Software]. *Zenodo*. https://doi.org/10.5281/zenodo.20664620

Savage, A., Arbic, B. K., Alford, M. H., Ansong, J. K., Farrar, J. T., Menemenlis, D., et al. (2017). Spectral decomposition of internal gravity wave sea surface height in global models. *Journal of Geophysical Research: Oceans*, *122*(10), 7803–7821. https://doi.org/10.1002/2017jc013009

Savage, A., Arbic, B. K., Richman, J. G., Shriver, J. F., Alford, M. H., Buijsman, M. C., et al. (2017). Frequency content of sea surface height variability from internal gravity waves to mesoscale eddies. *Journal of Geophysical Research: Oceans*, *122*(3), 2519–2538. https://doi.org/10.1002/2016jc012331

Shcherbina, A. Y., Sundermeyer, M. A., Kunze, E., D'Asaro, E., Badin, G., Birch, D., et al. (2015). The latmix summer campaign: Submesoscale stirring in the upper ocean. *Bulletin of the American Meteorological Society*, *96*(8), 1257–1279. https://doi.org/10.1175/bams-d-14-00015.1

Smith, L. M., & Waleffe, F. (2002). Generation of slow large scales in forced rotating stratified turbulence. *Journal of Fluid Mechanics*, *451*, 145–168. https://doi.org/10.1017/s0022112001006309

Spiro Jaeger, G., MacKinnon, J. A., Lucas, A. J., Shroyer, E., Nash, J., Tandon, A., et al. (2020). How spice is stirred in the bay of Bengal. *Journal of Physical Oceanography*, *50*(9), 2669–2688. https://doi.org/10.1175/jpo-d-19-0077.1

Tchilibou, M., Gourdeau, L., Morrow, R., Serazin, G., Djath, B., & Lyard, F. (2018). Spectral signatures of the tropical Pacific dynamics from model and altimetry: A focus on the meso/submesoscale range. *Ocean Science*, *14*(5), 1283–1301. https://doi.org/10.5194/os-14-1283-2018

Thomas, J., & Daniel, D. (2020). Turbulent exchanges between near-inertial waves and balanced flows. *Journal of Fluid Mechanics*, *902*, A7. https://doi.org/10.1017/jfm.2020.510

Thomas, J., Rajpoot, R. S., & Gupta, P. (2024). The turbulent cascade of inertia-gravity waves in rotating shallow water. *Journal of Fluid Mechanics*, *1000*, A30. https://doi.org/10.1017/jfm.2024.854

Thomas, J., & Yamada, R. (2019). Geophysical turbulence dominated by inertia-gravity waves. *Journal of Fluid Mechanics*, *875*, 71–100. https://doi.org/10.1017/jfm.2019.465

Thomas, L. N., Tandon, A., & Mahadevan, A. (2008). Submesoscale processes and dynamics. Ocean modeling in an eddying regime. *Geophysical Monograph Series*, *177*, 17–38.

Torres, H. S., Klein, P., Menemenlis, D., Qiu, B., Su, Z., Wang, J., et al. (2018). Partitioning ocean motions into balanced motions and internal gravity waves: A modeling study in anticipation of future space missions. *Journal of Geophysical Research: Oceans*, *123*(11), 8084–8105. https://doi.org/10.1029/2018jc014438

Vallis, G. K. (2006). *Atmospheric and oceanic fluid dynamics*. Cambridge University Press.

Vladoiu, A., Lien, R., & Kunze, E. (2024). Energy partition between submesoscale internal waves and quasigeostrophic vortical motion in the pycnocline. *Journal of Physical Oceanography*, *54*(6), 1285–1307. https://doi.org/10.1175/jpo-d-23-0090.1

Ward, M. L., & Dewar, W. (2010). Scattering of gravity waves by potential vorticity in a shallow-water fluid. *Journal of Fluid Mechanics*, *663*, 478–506. https://doi.org/10.1017/s0022112010003721

Warn, T. (1986). Statistical mechanical equilibria of the shallow water equations. *Tellus*, *38A*, 1–11. https://doi.org/10.3402/tellusa.v38i1.11693

Watanabe, M., & Hibiya, T. (2002). Global estimates of the wind-induced energy flux to inertial motions in the surface mixed layer. *Geophysical Research Letters*, *29*(8), 80. https://doi.org/10.1029/2001gl014422

Waterhouse, A., MacKinnon, J. A., Nash, J. D., Alford, M. H., Kunze, E., Simmons, H. L., et al. (2014). Global patterns of diapycnal mixing from measurements of the turbulent dissipation rate. *Journal of Physical Oceanography*, *44*(7), 1854–1872. https://doi.org/10.1175/jpo-d-13-0104.1

Whalen, C. A., de Lavergne, C., Naveira Garabato, A. C., Klymak, J. M., MacKinnon, J. A., & Sheen, K. L. (2020). Internal wave-driven mixing: Governing processes and consequences for climate. *Nature Reviews Earth & Environment*, *1*(11), 606–621. https://doi.org/10.1038/s43017-020-0097-z

Whitwell, C., Jones, N., Ivey, G., Rosevear, M., & Rayson, M. (2024). Ocean mixing in a shelf sea driven by energetic internal waves. *JGR: Oceans*, *129*(2), e2023JC019704. https://doi.org/10.1029/2023jc019704

Young, W., Rhines, P., & Garrett, C. (1982). Shear-flow dispersion, internal waves and horizontal mixing in the ocean. *Journal of Physical Oceanography*, *12*(6), 515–527. https://doi.org/10.1175/1520-0485(1982)012<0515:sfdiwa>2.0.co;2

Zeitlin, V. (2018). *Geophysical fluid dynamics: Understanding (almost) everything with rotating shallow water models*. Oxford University Press.

Zhurbas, V., & Oh, I. S. (2004). Drifter-derived maps of lateral diffusivity in the pacific and Atlantic oceans in relation to surface circulation patterns. *Journal of Geophysical Research: Oceans*, *109*(C5), C05015. https://doi.org/10.1029/2003jc002241